



HAL
open science

Repeating low frequency icequakes in the Mont-Blanc massif triggered by snowfalls

Agnès Helmstetter

► **To cite this version:**

Agnès Helmstetter. Repeating low frequency icequakes in the Mont-Blanc massif triggered by snowfalls. 2022. hal-03754592v1

HAL Id: hal-03754592

<https://hal.science/hal-03754592v1>

Preprint submitted on 19 Aug 2022 (v1), last revised 25 Nov 2022 (v2)

HAL is a multi-disciplinary open access archive for the deposit and dissemination of scientific research documents, whether they are published or not. The documents may come from teaching and research institutions in France or abroad, or from public or private research centers.

L'archive ouverte pluridisciplinaire **HAL**, est destinée au dépôt et à la diffusion de documents scientifiques de niveau recherche, publiés ou non, émanant des établissements d'enseignement et de recherche français ou étrangers, des laboratoires publics ou privés.

1 **Repeating low frequency icequakes in the Mont-Blanc**
2 **massif triggered by snowfalls**

3 **Agnès Helmstetter¹**

4 ¹ ISTerre, Univ. Grenoble Alpes, Univ. Savoie Mont Blanc, CNRS, IRD, Univ. Gustave Eiffel, 38000
5 Grenoble, France

6 **Key Points:**

- 7 • I have detected low frequency icequake signals with a main frequency of 5 Hz that
8 repeat every few minutes
9 • Low frequency icequakes mainly occur during and after snowfalls
10 • They are located on several glaciers of the Mont-Blanc massif mainly above 3000
11 m a.s.l. where ice is possibly cold

Corresponding author: Agnès Helmstetter, agnes.helmstetter@univ-grenoble-alpes.fr

12 Abstract

13 Deformation mechanisms of glaciers are highly sensitive to basal temperature; the
 14 motion of temperate glaciers is dominated by basal slip while cold-based glaciers deform
 15 mainly by internal creep. While basal slip is usually aseismic, unstable slip sometimes
 16 occurs and can be detected by seismometers. I have detected clusters of repeating low-
 17 frequency icequakes (LFIs) in the Mont-Blanc massif. Some properties of LFIs are sim-
 18 ilar to the high-frequency icequakes (HFIs) located at the base of Argentière glacier (*Helm-
 19 stetter et al., 2015*). Both HFIs and LFIs occur as bursts of tens to several thousand events,
 20 with typical inter-event times of several minutes and last for days or weeks. Unlike HFIs
 21 that have a broad spectra, LFIs have a characteristic frequency of about 5 Hz at all sta-
 22 tions, suggesting a rupture length of about 100 m. Seismic amplitudes and seismic wave-
 23 forms of LFIs progressively evolve with time within each cluster, suggesting changes in
 24 either rupture length or rupture velocity. Most LFIs are detected during snowfalls, while
 25 HFIs are not correlated with snowfalls. In this study, I used all available seismic stations
 26 within or around the Mont-Blanc massif between 2017 and 2022. I found LFIs located
 27 all over the massif but mainly above 3000 m. Some clusters are clearly associated with
 28 cold ice (near Mont-Blanc summit) while others below 2700 m a.s.l. are likely located
 29 under temperate glaciers and two clusters could be associated with landslides. This ob-
 30 servation of LFIs on cold glaciers is consistent with laboratory friction experiments sug-
 31 gesting that cold ice promotes unstable slip (*McCarthy et al., 2017; Saltiel et al., 2021;
 32 Zoet et al., 2018*).

33 1 Plain Language Summary

34 Glaciers flow due to slip at the base of the glacier and due to internal deformation.
 35 When the ice is at the melting point temperature, the presence of water at the base of
 36 the glacier promotes basal slip, while for cold ice (below melting temperature) the glacier
 37 is stuck to its bed and most deformation occurs within the glacier. The displacement of
 38 the glacier is usually slow and continuous, but in some cases slip can occur as intermit-
 39 tent fast slip events. These "icequakes" generate ground vibrations that can be recorded
 40 by seismic sensors. In this study, I analyze clusters of icequakes that repeat more or less
 41 regularly with time every few minutes, with progressive changes in amplitudes and inter-
 42 event times. The signals have a narrow spectrum with a main frequency of about 5 Hz
 43 that suggests a rupture length of about 100 m. These events mainly occur during snow-
 44 falls and are mostly located on glaciers above 3000 m. At these locations, the ice is of-
 45 ten colder than the melting point temperature. These repeating icequakes are probably
 46 associated with unstable slip at the base of glaciers. This result is surprising since basal
 47 motion for cold ice (below melting point) is believed to be negligible, but it is however
 48 consistent with laboratory experiments suggesting that unstable slip is promoted by cold
 49 temperatures. A few events occur on or close to glaciers at lower elevations, where ice
 50 is at the melting point temperature. They may be associated with basal glacier motion
 51 or with gravitational instabilities induced by glacier retreat.

52 2 Introduction

53 Basal icequakes have been observed under very different settings (ice-streams, out-
 54 let glaciers, alpine glaciers, ice-clad volcanoes), with hard-beds or basal till, over a huge
 55 range of scales (1 m - 200 km), rupture durations (from 0.1s to 30 mn), frequency con-
 56 tent (from 100 s to 500 Hz) and magnitude $-4 < m < 7$ (see for a review *Podolskiy
 57 and Walter (2016)*). Most of these events have a high waveform similarity, occur more
 58 or less regularly in time and display progressive changes in amplitude and recurrence times.
 59 Repeating basal icequakes are generally associated with stick-slip shear motion at "sticky-
 60 spots" at the ice-bed interface. The rupture area is stuck except during dynamic rup-
 61 ture (slip events). Stress decreases during slip events and increases between events due

62 to aseismic deformation. The nature of "sticky-spots" is difficult to identify. They could
 63 be associated with rock debris sliding over a hard bedrock (*Helmstetter et al.*, 2015) or
 64 with the ploughing of clasts embedded in the base of the ice through wet low diffusiv-
 65 ity till (*Barcheck et al.*, 2018). Another common point is that most of these events oc-
 66 curred under glaciers or ice-streams with temperate basal ice layer (ice at the melting
 67 point temperature), allowing aseismic slip around the "stick-spot" to reload the asper-
 68 ity between events.

69 Glacier basal motion is mainly controlled by the temperature of the basal layer and
 70 by the nature of the bed (*Cuffey and Paterson*, 2010). For temperate-based glaciers, basal
 71 motion accounts on average for half of the total motion. Basal motion is due to slip on
 72 the ice-bed interface for hard beds, while for soft beds most of basal motion is due to
 73 shear within the till layer. In contrast, cold glaciers with a basal layer below melting point
 74 are believed to deform mainly by viscous creep within the bulk of the glacier, with neg-
 75 ligible basal slip because ice is frozen to the bed.

76 The mechanisms responsible for stick-slip events are still debated. While basal seis-
 77 micity has mainly been observed so far for temperate basal ice, the only laboratory fric-
 78 tion experiments that reproduced unstable slip ("velocity-weakening" behavior) were us-
 79 ing ice samples below the freezing temperature (*McCarthy et al.*, 2017; *Saltiel et al.*, 2021;
 80 *Zoet et al.*, 2018). Basal icequakes can be triggered or modulated by tides (*Wiens et al.*,
 81 2008), snowfalls (*Allstadt and Malone*, 2014; *Thelen et al.*, 2013) and changes in basal
 82 water pressure (*Röösl, et al.*, 2016). Basal stick-slip motion is thus particularly infor-
 83 mative of glacier sliding processes and of basal properties (*Barcheck et al.*, 2018; *Kufner*
 84 *et al.*, 2021; *Smith*, 2006).

85 In this study, I report observations of repeating icequakes in the Mont-Blanc area.
 86 Repeating high frequency icequakes, with a mean frequency above 100 Hz, have previ-
 87 ously been detected under Argentière glacier in the Mont-Blanc massif (*Gimbert et al.*,
 88 2021; *Helmstetter et al.*, 2015). These events were associated with the repeated failure
 89 of rock debris over the bedrock. This study describes another type of repeating icequakes,
 90 with much lower average frequency of about 5 Hz. Both types of repeating icequakes oc-
 91 cur as bursts of events lasting for a few days or weeks, with progressive changes in inter-
 92 event times and amplitudes. But, unlike high frequency icequakes (HFIs), low-frequency
 93 repeating icequakes (LFI) occur mainly during or after snowfalls. They also occur at higher
 94 elevations, possibly associated with cold-based glaciers. These differences suggest that
 95 LFIs may be generated by a different physical mechanism.

96 **3 Study area and instrumentation**

97 **3.1 Mount-Blanc massif and Argentière glacier**

98 The Mont-Blanc massif extends over three countries (France, Italy and Swiss), cul-
 99 minates at 4807 m above sea level (a.s.l.), and includes about 155 km² of glaciers. There
 100 are both temperate valley glaciers with ice at the melting-point temperature (e.g., Mer
 101 de Glace and Argentière glaciers), polythermal (e.g., Tacconnaz and Tête Rousse glaciers)
 102 and cold hanging glaciers (e.g., Glacier de la Verte, Glacier de l'Aiguille du Tacul). Mer
 103 de Glace is the longest glacier of the massif; it culminates at 4248 m a.s.l. and flows down
 104 to about 1600 m a.s.l. over a length of about 12 km. Argentière glacier is the second largest
 105 glacier of the massif, with a length of 10 km and a maximum thickness of about 400 m.
 106 This glacier is particularly interesting as it has been studied since several decades with
 107 measurements of surface displacement and basal slip (*Vincent and Moreau*, 2016), sub-
 108 glacial water flow discharge, mass balance and meteorological data (*Vincent et al.*, 2009).
 109 In addition, several ground penetrating radar experiments, boreholes and seismic reflec-
 110 tion studies provided accurate information on the topography of the bedrock and on the
 111 seismic wave velocities (*Gimbert et al.*, 2021). Although our goal was initially to ana-

112 lyze icequake activity on Argentière glacier, I found out that most detected events did
 113 not occur on Argentière glacier but were distributed all over the Mont-Blanc massif.

114 3.2 Seismic stations

115 I used all available temporary and permanent seismic stations in the Mont-Blanc
 116 area. Table 1 gives the characteristics of each station used in this study. The stations
 117 inside the Mont-Blanc massif are shown in the map in Figure 11.

118 Several seismological experiments have been performed on Argentière glacier since
 119 2017. A few seismic stations have been operated between October 2017 and May 2020
 120 (stations B01-B04), with several gaps in the acquisition. The first station B01 was in-
 121 stalled on Argentière glacier on 2017/10/4 at 2392 m a.s.l. (*Nanni et al.*, 2020). Then
 122 station B02 was installed at 70 m depth in a borehole close to B01 on 2018/4/20, fol-
 123 lowing with B03 on 2018/10/23 at 2657 m a.s.l. and B04 on 2019/6/26 at 2524 m a.s.l.

124 Two other temporary seismic stations were in acquisition in summer or autumn
 125 2021. Station DOM was located near Col du Dôme (45.8422°N, 6.8466°E, 4243 m a.s.l.)
 126 and station MDG on Mer de Glace (45.9203°N, 6.9264°E, 1897 m a.s.l.).

127 Two temporary one-month experiments with a larger number of sensors have been
 128 performed. From 2018/4/20 until 2018/5/31, the lower part of Argentière glacier has been
 129 instrumented with a network of 98 seismometers (stations AR001-AR100). The prelim-
 130 inary results of this experiment have been described by *Gimbert et al.* (2021) and the
 131 data is available from *Roux et al.* (2021). Another short-term experiment has been con-
 132 ducted from 2019/12/5 until 2020/1/10 using 13 sensors distributed in 3 antennas (*Helm-
 133 stetter*, 2020). An antenna of 5 sensors (N11-N15) was located at Col des Grands Mon-
 134 tets at about 3260 m a.s.l. with a distance between sensors of about 100 m. Another an-
 135 tenna of four sensors was located near station B03 at about 2650 m a.s.l. (N21-N24), and
 136 the last antenna was located near B04 at about 2500 m a.s.l. (N31-N34). All these sen-
 137 sors lost their GPS signal after being started in Chamonix on 2019/12/4 and before in-
 138 stallation on the glacier the next day. I was not aware that these sensors should not be
 139 moved after acquisition starts. I thus used local earthquake signals in order to correct
 140 the clock drift, which reached about 1 s after one month. I found a timing accuracy of
 141 about 0.02 s which is not sufficient to use beam-forming methods. I thus selected only
 142 one sensor out of each antenna (N13, N21 and N31).

143 Station BLANC was installed within the Mont-Blanc massif near Torino Refuge
 144 at an elevation of 3379 m on 2019/6/14. I also used data from stations around the Mont-
 145 Blanc massif. Stations CI17-CI23 of the CIFALP project (*Zhao et al.*, 2018) were in op-
 146 eration between 2018/11/11 - 2019/12/3. Stations CI18-CI20 were reinstalled at the same
 147 location on 2019/12/20 (*Helmstetter and Guéguen*, 2020). Three stations (MFERR, VFER2
 148 and AMID2) were installed by ETH Zurich in 2019 to detect and locate earthquakes in
 149 the Mont-Blanc massif. I also used permanent stations located further away: stations
 150 SEMOS, DIX, AIGLE, ILLEZ, SENIN, GRYON, FULLY, SALAN from the Switzerland
 151 Seismological Network (*Swiss Seismological Service*, 1983), Italian stations REMY, CIRO,
 152 LSD (*University of Genova*, 1967) and MRGE (*INGV*, 2006), and stations RSL and OGS
 153 in France (*RESIF*, 1995).

154 3.3 Snow falls and atmospheric pressure

155 I used meteorological data to analyze the influence of precipitations and atmospheric
 156 pressure on the occurrence of LFIs. A permanent meteorological station is installed on
 157 a moraine above Argentière glacier near 2400 m a.s.l. as part of GLACIOCLIM obser-
 158 vatory (*Six and Vincent*, 2014). However this station does not measure snow falls . The
 159 closest station that measures snow falls is a meteofrance station located outside the Mont-
 160 Blanc massif, in the Aiguilles Rouges massif, at 2365 m a.s.l. But there are many gaps

Table 1. Characteristics of all seismic stations used in this study

Name	Network code	Time interval	Sensor	Cut-off frequency	Sampling rate (Hz)
B01		2017/10/4-2018/9/13	Geobit-C100-MK2	10 s	1000
B02		2018/4/18-2019/2/4, 2019/7/16-2019/10/16, 2019/12/6-2020/5/11	Geobit S 400 C	1 Hz	1000 100 100
B03		2018/10/23-2019/3/22, 2019/3/23-2019/5/14, 2019/6/25 -2020/1/27	Geobit C100-MK2	10 s	1000 100 1000
B04		2019/6/26-2020/1/25	Geobit C100-MK2	10 s	100
DOM		2021/7/2-2021/8/28	Geobit S-100 1C	4.5 Hz	800
MDG		2021/9/18-2021/12/18	Geobit C100 3C	4.5 Hz	100
AR001-100	ZO	2018/4/25-2018/5/31	Fairfield ZLand 3C	4.5 Hz	500
N11-35	1D	2019/12/5-2020/1/10	Fairfield ZLand 3C	4.5 Hz	250
CI17-CI23	XT	2018/11/11-2019/12/3	Trillium Horizon	120 s	100
CI18-CI20	8C	since 2019/12/20	Guralp CMG40	40 s	200
MFERR	8D	since 2019/5/28	Lennartz LE-3D	1 s	100
AMID2, VFER2	8D	since 2019/12/4	Lennartz LE-3D	1 s	200
BLANC	GU	since 2019 06 14	Trillium 40s	40 s	100
REMY, LSD, CIRO	GU	since 2011 or before	Trillium 40s	40 s	100
MRGE	IV	since 2005/6/24	Trillium 40s	40 s	100
SEMOs	CH	since 2013/6/18	EpiSensor ES-T	none	250
DIX, AIGLE.	CH	since 2018 or before	Streckeisen STS2	120 s	200
SENIN, SALAN	CH	since 2018 or before	Streckeisen STS2	120 s	200
ILLEZ, FULLY	CH	since 2018 or before	Trillium Compact	120 s	100
GRYON	CH	since 2002/10/2	Trillium 240s	240 s	200
OGSI	FR	since 2016/6/15	Trillium Compact	20 s	200
RSL	FR	since 2010/5/28	Trillium 120PA	120 s	100

161 in the snow fall data during snow fall episodes. Therefore, I use data from the S2M database
 162 (*Vernay et al.*, 2019), which provides a reanalysis of meteorological and snow cover data.
 163 This model adjusts a guess from a numerical weather prediction model with the best pos-
 164 sible set of available in-situ meteorological observations. It provides the hourly rate of
 165 snowfall on the Mont-Blanc massif for different ranges of elevations and slope orienta-
 166 tions.

167 The GLACIOCLIM station only measures atmospheric pressure since 2019/9/13.
 168 Before this date, I use data from the closest MeteoFrance station that measures atmo-
 169 spheric pressure located at Bourg Saint Maurice 24 km South from Mont-Blanc. I checked
 170 that both stations provide similar values after shifting the Bourg Saint Maurice pressure
 171 to correct the effect of elevation. When both stations are in operation the correlation
 172 coefficient between the pressure estimated at Argentière and Bourg-Saint-Maurice is 0.88.

173 4 Methods

174 4.1 Detection, classification and selection of repeating LFIs

175 I detected a first sequence of low-frequency icequakes by simply screening a one-
 176 hour long signal recorded by station B01 on 2017/12/19 at 22:00 UTC. In Figure 1, we
 177 can see very regular peaks in the seismogram repeating on average every 160 s. Signals
 178 are highly similar, with a duration of about 5 sec, an average frequency around 5 Hz and
 179 no high frequency energy. Once we identify one event, it is straightforward to detect sim-
 180 ilar events using the template-matching method (*Gibbons and Ringdal*, 2006). I first used
 181 this method with a relatively low correlation threshold (0.4), a time window of 5 s, a band-
 182 pass filter of 2-20 Hz, using the three components of station B01. By screening the wave-
 183 forms of detected events, I noted significant and abrupt changes in the waveforms and
 184 amplitudes. I thus divided the set of detected events into different clusters using the hi-
 185 erarchical agglomerative clustering method with average linkage (*Sokal and Michener*,
 186 1958).

187 In order to perform a more systematic detection, I applied the STA/LTA algorithm
 188 of *Allen* (1978) on all the data at the reference station using a signal-to-noise ration of
 189 3 and a bandwidth filter between 3 and 10 Hz. I used different reference stations for dif-
 190 ferent periods: B01 (2017/10/4 - 2018/6/12), B03 (2018/10/23 - 2019/9/11), N21 (2019/12/5
 191 - 2020/1/10), B02 (2020/2/8 - 2020/5/12) and BLANC (2019/6/14 - 2022/6/1). I de-
 192 tected on average more than 300 events per day, with a large variability in amplitude,
 193 frequency content and signal duration, likely produced by different processes (crevasse
 194 opening, basal slip, avalanches, rockfalls, earthquakes, noise...). The number of detected
 195 events was much too large (several hundred thousand events) to apply the hierarchical
 196 clustering method in order to group events into clusters with similar waveforms. I thus
 197 screened manually the catalog to identify bursts of events with similar amplitudes and
 198 duration and quasi-periodic recurrence times. I also applied the hierarchical clustering
 199 method on all large events (peak ground velocity larger than 10 $\mu\text{m/s}$) to make sure that
 200 I did not miss any cluster of large amplitude signals.

201 This way I identified several thousand clusters of low-frequency signals for the whole
 202 time period. Within each identified cluster, I computed the average signal and used this
 203 stacked signal as the new template signal for this cluster. When the correlation between
 204 different templates was larger than 0.9, I merged the clusters. I then applied the template-
 205 matching algorithm on the continuous data at the reference stations with a correlation
 206 threshold of 0.5. I used different signal durations for different clusters (2, 3 or 5 s), start-
 207 ing about 0.5 s before the first arrival and ending just after the last visible arrival. If an
 208 event was detected by several templates, I chose the one with the largest correlation.

209 In this work, I am interested in detecting "low-frequency" repeating icequakes (LFIs)
 210 similar to those shown in Figure 1. Here, the term "low-frequency" means average fre-

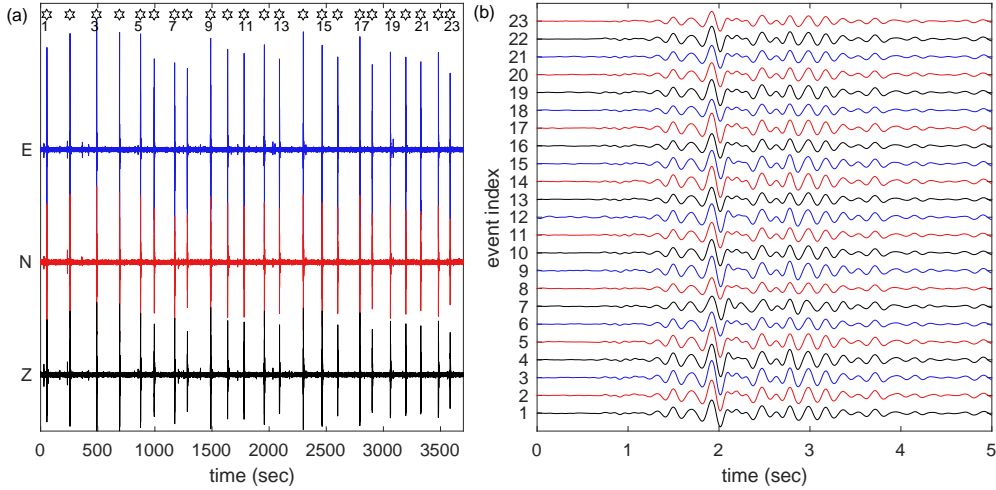


Figure 1. a) Seismic signal recorded by station B01 on 2017/12/19 at 22:00 UTC bandpass filtered between 1 and 20 Hz. LFIs are highlighted by stars. The corresponding seismograms for each event are shown in b) for the East component.

211 frequencies of about 5 Hz, much lower than the average frequency of about 50 Hz for the
 212 high-frequency basal icequakes (HFIs) located below the lower part of Argentière glacier
 213 near 2350 m a.s.l. (*Gimbert et al., 2021; Helmstetter et al., 2015*). The definition of "re-
 214 peating" events is also delicate (*Uchida and Bürgmann, 2019*). Here I consider repeaters
 215 as events occurring quasi-periodically in time, i.e., that are more regular than a Pois-
 216 son random process (with uniform rate in time). I do not impose that they rupture the
 217 same asperity, as the location accuracy is not good enough compared to the rupture length.

218 Regularity in time is usually characterized by the coefficient of variation (ratio of
 219 standard deviation over average recurrence time), with a value equal to 1 for a Poisson
 220 process, smaller than 1 for quasi-periodic occurrence times and larger than one for clus-
 221 tered events. But the coefficient of variation does not provide a good way to identify re-
 222 peating icequakes. Repeating LFIs occur as bursts of activity separated by quiescent peri-
 223 ods, as observed before for HFIs (*Helmstetter et al., 2015*). During active periods, both
 224 the inter-event times and the amplitude evolve progressively in time. The coefficient of
 225 variation is thus often larger than one, due to the succession of active phases and peri-
 226 ods of very low activity (possibly misclassified events) and to progressive changes in re-
 227 currence time. To account for slow changes in activity rate, I normalize each recurrence
 228 time by the median value over a sliding window of 10 events. I also replace the standard
 229 deviation by the median absolute deviation, which is less sensitive to extreme events. Our
 230 modified "coefficient of variation" is thus defined as $median(|dt^* - 1|)$, where dt^* is the
 231 normalized recurrence times. I select all clusters with a coefficient smaller than 0.5, sig-
 232 nificantly smaller than values in the range 0.6-0.7 obtained for Poissonian synthetic cat-
 233 alogs.

234 During quiet phases between bursts of LFIs, events usually have a smaller correla-
 235 tion with the template than during bursts for the same peak amplitude. These isolated
 236 events may thus have a slightly different location or be due to a different triggering fac-
 237 tor. I thus remove these isolated events before attempting to locate them or to analyze
 238 the correlation with potential triggering factors. For each cluster of repeaters, I remove
 239 events with inter-event times larger than 10 times the median value. A cluster is thus
 240 divided in several temporal sub-clusters, separated by gaps longer than 10 times the me-

241 dian inter-event time. In order to limit the number of sub-clusters, I then merge together
 242 sub-clusters if the gap is less than 1/4 of the duration of the smallest sub-cluster.

243 4.2 Localization

244 4.2.1 *Stacking and picking signals*

245 I attempted to locate each cluster of LFIs by manually picking P and S phases at
 246 a maximum of stations. Since individual events are rarely visible at stations outside the
 247 glacier, I stacked the signals for a selection of events for each cluster. For large clusters
 248 with more than 1000 events, I selected only the 1000 best events, with the largest am-
 249 plitude and correlation with the template signal at the reference station. For all clus-
 250 ters I selected events that occurred during the bursts, because events that occurred iso-
 251 lated in time during quiet periods are more likely to be false detections and to come from
 252 a different source. Specifically, I computed the median recurrence time and removed events
 253 with inter-event time larger than 10 times this value. Signals were first bandpass filtered
 254 between 2 and 20 Hz. Instead of using the average over all selected events, I used the
 255 median signal because it improves the signal-to-noise ratio by removing the influence of
 256 outliers (*Allstadt and Malone, 2014*). This helps to reduce the influence of noisy signals
 257 or false detections. Before taking the median, I removed events with a very large noise
 258 amplitude, e.g., due to anthropogenic noise, instrumental issues or noise due to water
 259 flow. I computed the average noise amplitude over a time window of 20 s before each event
 260 and removed events with a noise amplitude larger than twice the median value.

261 I then manually picked first arrivals of P and S waves at all available stations listed
 262 in Table 1 when I could visually identify these phases. For the three node antennas in-
 263 stalled in December 2019 (stations N11-N15, N21-N24, N31-N34), I selected only one sta-
 264 tion for each antenna (nodes N11, N21 and N31). Because of the small inter-node dis-
 265 tance (about 100 m), large source-node distance (several kms) and clock errors for these
 266 stations, I believe including more sensors would not improve the location accuracy. In
 267 order to keep only the best constrained locations, I selected only clusters with a min-
 268 imum of 7 phases picked at a minimum of 4 stations and also imposed at least one sta-
 269 tion outside the glacier. I did not use data from the nodes AR001-AR100 installed in
 270 April-May 2018 during Resolve experiment. These nodes detected only two clusters of
 271 LFI but these clusters could not be located accurately because they were not detected
 272 by stations outside the glacier.

273 4.2.2 *Velocity model*

274 Tomographic studies in the Alps do not have a good enough resolution and are not
 275 adapted to our study of shallow sources because they do not estimate seismic wave ve-
 276 locity above sea level. Therefore, I used phase arrivals from swarms of micro-earthquakes
 277 in the Mont-Blanc area in order to estimate average P and S wave velocities. I selected
 278 1710 earthquakes detected by the regional seismological network Sismalp from 2017/1/1
 279 until 2021/1/27 with latitude in the range 45.8-46°N and longitude between 6.8 and 7.1°E.
 280 Most of these events were part of a swarm located below the Grandes Jorasses summit
 281 at about 5 km depth below sea level, while another smaller swarm was located under Aigu-
 282 ille du Midi. For each station in Table 1 and for each earthquake I computed apparent
 283 P and S velocities from earthquake source times and phase arrivals. I then took the av-
 284 erage over all events at each station and then averaged over all stations. This yielded
 285 $V_P = 5.68$ km/s and $V_S = 3.41$ km/s. Since icequakes are quite shallow and located
 286 at a larger elevation than most stations, I account for the surface topography to avoid
 287 ray paths in the air. I use NASA SRTM digital elevation data with a resolution of 30
 288 m (*Jarvis et al., 2008*). Our 3D velocity model is homogeneous below the surface and
 289 has $V_P = 0.34$ km/s and $V_S = 0.01$ km/s in the air. V_S needs to be positive in the
 290 air but its value has no influence on the results as long as $V_S \ll 1$ m/s. It covers the

291 Mont-Blanc massif and extends further away to include all seismic stations listed in Ta-
 292 ble 1. The grid spacing is fixed to 100 m in all directions and the depth ranges between
 293 0 and 5 km a.s.l.. I cannot decrease the resolution because the size of the 3D velocity
 294 model of dimension $5 \times 100 \times 100$ km would be very large and the computing time too
 295 long.

296 Seismic wave velocities in the ice are significantly smaller than in the bedrock ($V_P =$
 297 3.62 km/s, $V_S = 1.83$ km/s) (*Gimbert et al.*, 2021). For stations located on glaciers,
 298 this can thus yield notable errors in the estimated travel times. However, the geometry
 299 of glaciers is not well known, except for Argentière glacier. But I cannot include the ice
 300 layer in the velocity model due to its limited resolution in space (grid size of 100 m). I
 301 thus use station corrections to minimize these errors.

302 **4.2.3 Station corrections**

303 Station corrections can account for un-modeled heterogeneities in the seismic wave
 304 velocities. Many stations are located on Argentière glacier above several hundred met-
 305 ters of ice. I estimated time corrections for these stations by computing travel-times in
 306 the velocity model described above ($V_P = 5.68$ km/s, $V_S = 3.41$ km/s below the sur-
 307 face) and in a 3D model accounting for different velocities within Argentière glacier. The
 308 geometry of the glacier is defined by a synthesis of radar and seismic profiles (*Gimbert*
 309 *et al.*, 2021). The seismic wave velocities in the ice ($V_P = 3.62$ km/s, $V_S = 1.83$ km/s)
 310 were inverted from the localization of high-frequency basal icequakes detected by the Re-
 311 solve experiment (*Gimbert et al.*, 2021). I then estimated travel times for each velocity
 312 model (with and without glacier) on a rectangular grid covering the Argentière glacier
 313 (longitude between 6.956° and 7.046° E, latitude between 45.913° and 45.97° N) with a grid
 314 spacing of 30 m, for each station on the glacier and for each grid point. The time delay
 315 between the two model varies in space but is relatively homogeneous outside the Argentière
 316 glacier and at large distance from the station. The time correction for each station is thus
 317 defined as the average time delay for grid points located at the surface outside the glacier
 318 and south-west from the glacier. I do not include grid points located within the north-
 319 ern part of the grid because I found very few icequakes in this area and because the time
 320 delay computed for station N13 (near Col des Grands Montets) is very different for points
 321 located south or north from Argentière glacier (i.e., for ray paths that do or do not cross
 322 the glacier). The maximum time delay of 0.14 s is obtained for S waves at station B04,
 323 where the glacier thickness is the largest reaching about 450 m.

324 **4.2.4 Location method**

325 I use NonLinLoc location method (*Lomax et al.*, 2000), which uses a probabilis-
 326 tic location method providing more accurate estimates of location errors. This method
 327 provides the most likely location as well as a scatter of possible solutions. This is par-
 328 ticularly interesting when there are multiple local minima of time residuals. I use the
 329 3D velocity model described above and station corrections for stations on the glacier.
 330 I assume gaussian picking errors with a standard error of 0.1 s for both P and S waves.
 331 and minimize the root-mean-square residuals. The inversion is performed using the Oct-
 332 tree Importance Sampling Algorithm as it is much faster than a grid-search. The topog-
 333 raphy of the area is used to search for possible sources located only below the ground
 334 surface.

335 **4.3 Magnitude**

336 Among all types of magnitudes, the moment magnitude is generally preferred as
 337 it directly depends on physical source properties, rupture area and slip. However, it is
 338 difficult to estimate moment magnitude for our signals because they have a limited fre-
 339 quency range, a very small signal-to-noise ratio for most events and for stations outside

340 the Mont-Blanc massif and are likely dominated by surface waves. I thus estimated both
 341 the surface-wave magnitude M_s and the local magnitude M_l .

342 I used the definition of the surface-wave magnitude given by *Bormann and Dewey*
 343 (2014)

$$M_s = \log_{10}(A/2\pi) + 1.66 \log_{10} \Delta + 0.3, \quad (1)$$

344 where A is the maximum amplitude of the surface-wave on the vertical trace and Δ is
 345 the epicentral distance in degrees. Note that I use this definition of M_s out of its rec-
 346 ommended range of frequencies (3-60 s) and epicentral distance ($2 < \Delta < 60^\circ$).

347 The local magnitude is given by (*Bormann and Dewey, 2014*)

$$M_l = \log_{10}(A_d) + 1.11 \log_{10}(d) + 0.00189d - 2.09 + C, \quad (2)$$

348 where A_d is the amplitude in nm of the horizontal displacement seismogram that would
 349 have been recorded on a Wood-Anderson seismometer and d is the hypocentral distance
 350 (in km). This definition of M_l is only valid for crustal earthquakes in regions with at-
 351 tenuation properties similar to those of Southern California (*Bormann and Dewey, 2014*),
 352 I thus added a corrective term C . I estimated the correction term $C = 0.4$ to match
 353 the local magnitude of local earthquakes detected by Sismalp and computed using seis-
 354 comp software, for a selection of 30 earthquakes located in the Mont-Blanc massif with
 355 $0 < M_l < 3.1$ between 2018/12/21 and 2021/1/23.

356 For each cluster, I compute the magnitudes M_l and M_s of the largest event that
 357 occurred during active phases (rejecting isolated events). However, even the largest event
 358 is not always visible on all stations where this cluster was picked due to the weak signal-
 359 to-noise ratio. I thus applied the following procedure to estimate the amplitude A of the
 360 largest event at each station. For each station, I compute the amplitude A_i of each event
 361 i by computing the scaling amplitude factor between the signal y_i and the stacked sig-
 362 nal y_s (*Gibbons and Ringdal, 2006; Schaff and Richards, 2011*)

$$A_i = A_s \frac{\sum_{j=1}^N y_i(t_j) y_s(t_j)}{\sum_{j=1}^N y_s(t_j)^2}, \quad (3)$$

363 where y_s is the vertical component of the stacked signal, A_s is its peak amplitude and
 364 the time index j varies from 2 s before until 2 sec after the time of the peak amplitude
 365 of the stacked signal. This greatly improves the accuracy of the estimated peak ampli-
 366 tude for repeating signals, but is often still unreliable when the signal is buried in the
 367 noise. I thus fit a linear regression between the peak amplitude estimated at the refer-
 368 ence station (B01, B02, B03 or BLANC) and at each other station, after selecting events
 369 that have a correlation with the stacked signal greater than its median value. This helps
 370 to remove noisy events and to obtain a more accurate value for the peak amplitude of
 371 the largest event of each cluster at each station.

372 5 Results

373 5.1 Characteristics of Seismic Signals

374 There are many different types of icequakes that have been detected on Argentière
 375 glacier (*Gimbert et al., 2021; Helmstetter et al., 2015*). Even when focusing on repeat-
 376 ing basal events, I found very different frequency ranges, from HFIs with energy above
 377 500 Hz located at a few hundred meters from the sensor (*Gimbert et al., 2021; Helmstet-
 378 ter et al., 2015*), to the LFIs described in this study. However, It is not clear wether the
 379 frequency content represents the frequency of the source process or if the signal is strongly
 380 affected by attenuation that depletes the signal in high-frequencies.

381 Figure 2 compares the seismograms and spectrums of low- and high-frequency re-
 382 peating icequakes with a local earthquake recorded at station B01. The LFI signal has

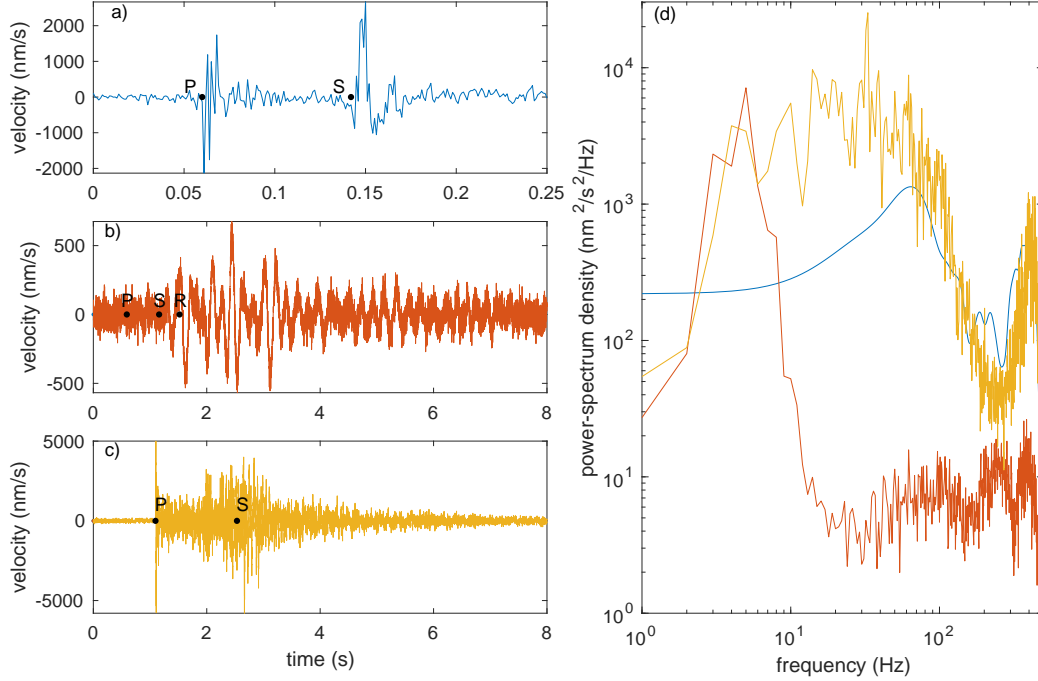


Figure 2. Seismograms of (a) a high-frequency icequake, (b) a low-frequency icequake and (c) a $M_l = 1.1$ local earthquake detected at station B01. Signals are vertical ground motion high-pass filtered at 1 Hz. Arrival times of P, S and surface waves ('R' in(b)) are shown by dots. The corresponding spectrums are shown in (d) for the high-frequency icequake in blue, low-frequency icequake in red and local earthquake in yellow.

383 less energy above 6 Hz compared with a local earthquake of $M_l = 1.1$ detected at a distance of 10 km, whereas the LFI is located closer at about 3.5 km from the sensor. This
 384 suggests that the lack of high frequency energy for the LFI could be a source property.
 385 However, the LFI is much shallower than the earthquake, so that attenuation is likely
 386 stronger for the LFI than for the earthquake located at 3.4 km below sea level. More-
 387 over, the LFI signal is mainly composed of surface waves, which always have lower fre-
 388 quencies than body waves. But I don't think that these effects could explain the sharp
 389 decrease in the LFI spectrum above 6 Hz and the huge difference in high frequency en-
 390 ergy above 10 Hz between the LFI and the earthquake.
 391

392 Distinguishing the different phases for the LFI shown in Figure 2b is delicate. The
 393 different waves (P, S and Rayleigh waves) are more easily identified when bandpass fil-
 394 tering the data between 2 and 10 Hz, stacking over all events of the same cluster and look-
 395 ing at the signal polarization (see Figure 3).

396 5.2 Temporal Evolution

397 Clusters of repeating LFIs are generally active for a few hours or days. The same
 398 cluster can however reappear a few days or months latter. Figure 4 displays the tempo-
 399 ral evolution of repeating events during one of the most active periods between 2018/10/27
 400 and 2018/11/9. This figure only shows the 7 clusters with at least 1000 events during
 401 this time period. In addition, I also plot a smaller cluster of 190 events that displays a
 402 highly regular pattern and longer recurrence times (black dots in Figure 4). This figure
 403 illustrates the typical patterns as well as discrepancies between clusters. Clusters usu-

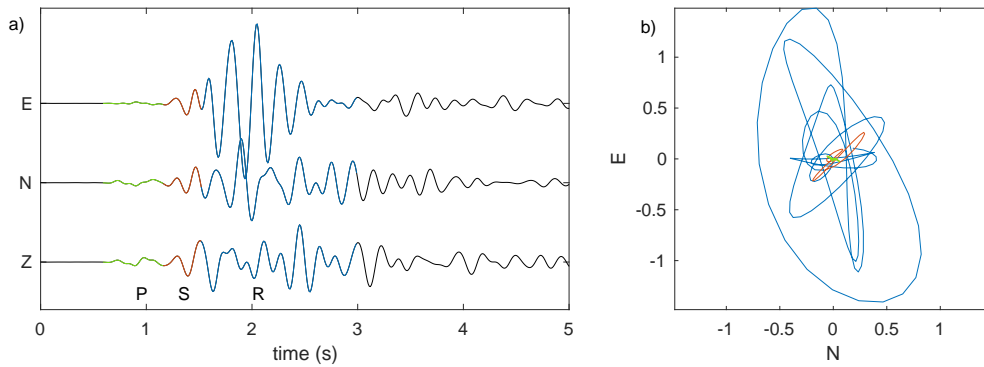


Figure 3. (a) Seismograms of the stacked signal for one cluster of LFIs detected at station B01 bandpass filtered between 2 and 10 Hz. (b) Velocity ground motion in the horizontal plane. I used a different color for each wave, P wave in green, S wave in red and surface waves in blue.

404 ally start as very small events with short and irregular occurrence times. But during the
 405 beginning of the cluster many small events are likely missed. In a second phase, both
 406 the amplitudes and the recurrence times increase in time and become more regular. Some
 407 sequences then stop abruptly or slow down slowly with a progressive decrease in ampli-
 408 tudes and increase in recurrence times. Different clusters stop and end at different times.
 409 I found no correlation between the LFI occurrence times between different clusters. This
 410 suggests that they are not interacting with each other and that the triggering factors or
 411 the "nucleation time" of clusters differ.

412 5.3 Correlation with snowfalls

413 Figures 5 and 6 compare the snowfalls and the rate of repeating LFIs for two time
 414 periods. Repeaters are mostly observed between October and May. Few events are ob-
 415 served in summer but they could be hidden by the increase in seismic noise during the
 416 melting period. Most bursts of repeaters coincide with snowfalls. This is confirmed by
 417 computing the cross-correlation between the snow-fall rate and the rate of repeating events
 418 shown in Figure 7. The cross-correlation function shows a peak for positive times (ice-
 419 quakes occurring after snowfalls) with a maximum at 1.6 days and returns to zero af-
 420 ter 10 days. Smaller and broader peaks for negative times are spurious and result from
 421 peaks in the autocorrelation of snowfall data. LFIs are also negatively correlated with
 422 atmospheric pressure. This is surprising since decreasing the atmospheric pressure should
 423 have the same effect as decreasing the snow load. If snow load triggers LFIs, then in-
 424 creasing atmospheric pressure should also trigger LFIs. Atmospheric pressure is also strongly
 425 anti-correlated with snowfall rate (black curve in Figure 7) so that it is difficult to dis-
 426 entangle the relative effect of atmospheric pressure and snow load on the triggering of
 427 LFIs. Changes in atmospheric pressure and snowfall load have indeed the same order
 428 of amplitude. I have analyzed the average temporal evolution of atmospheric pressure,
 429 snowfall load and the rate of LFIs during snowfall episodes. I have selected 29 snowfall
 430 episodes with a weight larger than 1 hPa that started at least 3 days after the end of the
 431 previous episode. I then stacked each variable for all snowfall episodes relative to the time
 432 of peak snowfall rate (see Figure 8). The results show that the snow load increases on
 433 average by 7 hPa three days after the peak of snowfall compared to its value three days
 434 before the peak. During the same time interval, atmospheric pressure decreases by 8 hPa
 435 and reaches its minimum value when the snowfall rate is maximum. It then recovers up

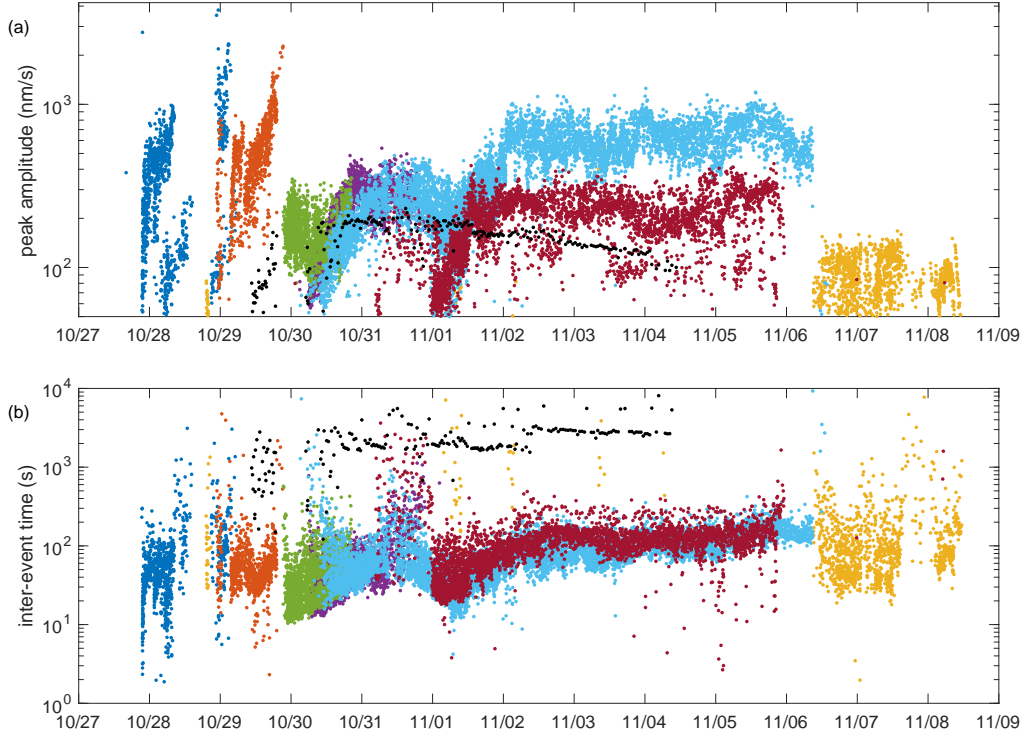


Figure 4. Temporal evolution of peak amplitude (a) and recurrence time (b) for a selection of 8 different clusters of repeaters between 2018/10/27 and 2018/11/9.

436 to -3 hPa three days after the peak of snow rate. Summing snow load and atmospheric
 437 pressure, the average effect on normal stress change is thus positive for times larger than
 438 one day after the peak of snowfall rate. The average rate of LFIs is larger than average
 439 for positive times, when both atmospheric pressure and snow load increase. Note how-
 440 ever that this describes the average behavior but that individual sequences can differ widely
 441 from this typical pattern.

442 Figure 9 further confirms that LFIs occur predominantly during snowfalls, but also
 443 during times of low atmospheric pressure and when pressure increases. Figure 9 shows
 444 the probabilities distribution function (pdf) of atmospheric pressure, hourly atmospheric
 445 pressure change, and snowfall rate. It compares the pdfs at all times during seismic ac-
 446 quisition (blue curves) and at times of LFIs (red curves). LFIs are roughly two or three
 447 times more frequent than average during snowfalls and when atmospheric pressure is lower
 448 than 750 hPa. The change in atmospheric pressure has a smaller impact on the occur-
 449 rence of LFIs, with the rate of LFIs increasing by 21% when the atmospheric pressure
 450 increases (Figure 9b).

451 I also estimated the relation between the cumulated snowfall weight during each
 452 snowfall episode and the rate of repeaters (Figure 10). I defined snowfall episodes from
 453 the snowfall hourly data as consecutive days (24 hrs) with a positive snowfall rate sepa-
 454 rated by at least 24 hrs without snow. Clusters were separated into temporal sub-clusters
 455 as described in section 4.1. For each snowfall episode, I selected sub-clusters that initi-
 456 ated after the beginning of the snowfall and I count all events of the sub-cluster un-
 457 til 10 days after the peak of snowfall rate, even after the end of the snowfall episode. Both
 458 the number of events and the number of clusters increase roughly exponentially with the
 459 cumulated snowfall weight. The correlation coefficient is $R = 0.52$ for the number of

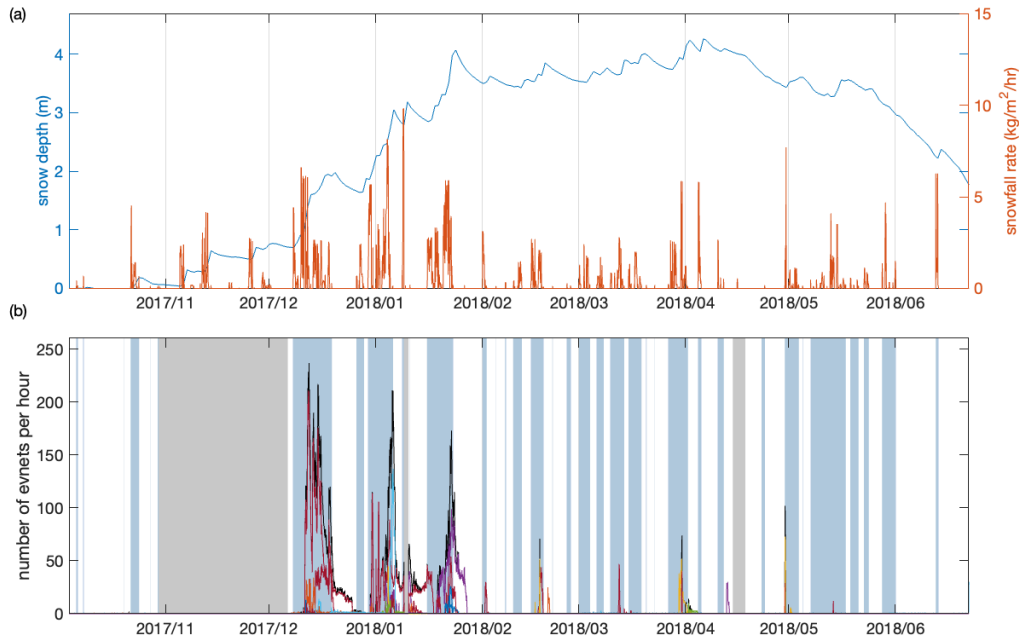


Figure 5. (a) Temporal evolution of snow depth and snow rate and (b) rate of repeating events detected at station B01. Blue shaded areas indicate snowfall episodes and grey areas data gaps. Different colors indicate different clusters. The black curve represent the sum over all clusters.

460 events and $R = 0.60$ for the number of clusters. These correlations are significant at
 461 the 99% confidence level. There is however a considerable scatter around this trend, many
 462 snowfall episodes not triggering repeaters. The magnitude of LFIs shows no significant
 463 correlation with the snowfall weight.

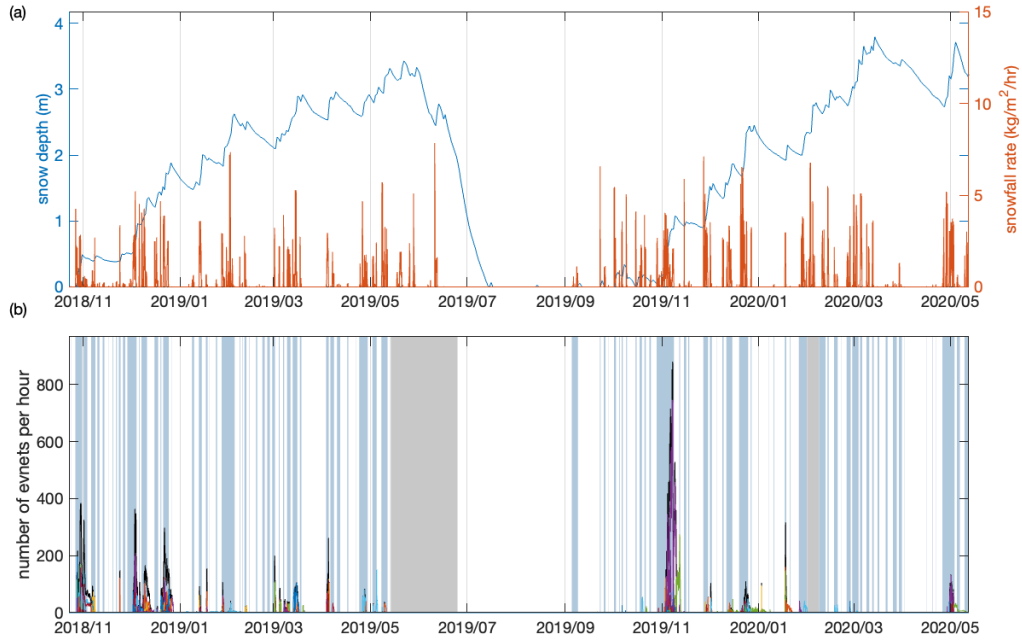


Figure 6. Same as Figure 5 for the time period 2018/10/23-2020/5/12. a) Temporal evolution of snow depth and snow rate and (b) rate of repeating events detected at station B03 before 2020/1/28 and at station B02 after 2020/1/28.

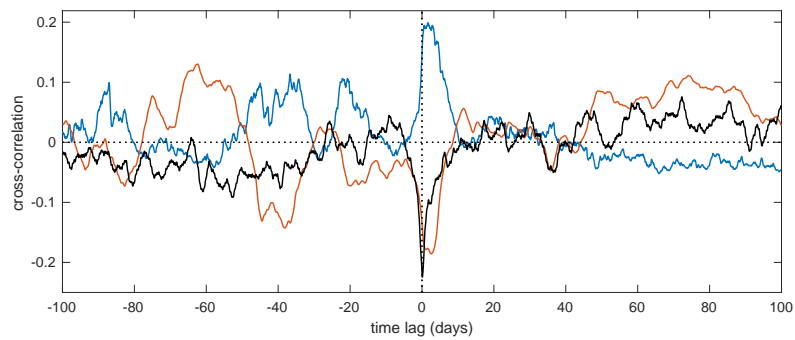


Figure 7. Normalized cross-correlation function between snowfall rate and hourly rate of LFIs for the time period 2017/10/4-2020/5/12 in blue, between hourly rate of LFIs and atmospheric pressure in red, and between atmospheric pressure and snowfall rate in black.

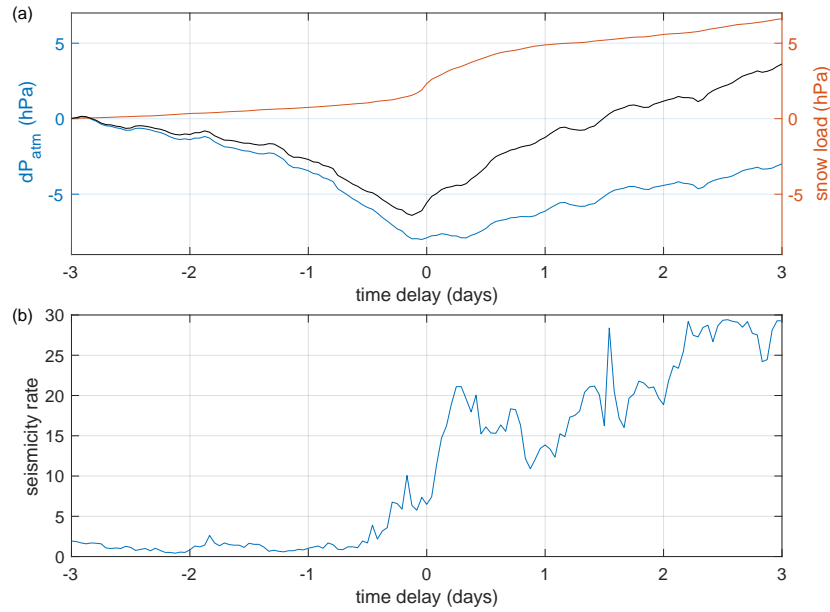


Figure 8. Average temporal evolution of (a) snow-fall weight in red, atmospheric pressure in blue, sum of these two terms in black and (b) rate of LFIs, stacking over 29 selected snowfall episodes with a total weight larger than 1 hPa (10 kg/m^2) and aligned in time relative to the peak of snowfall rate.

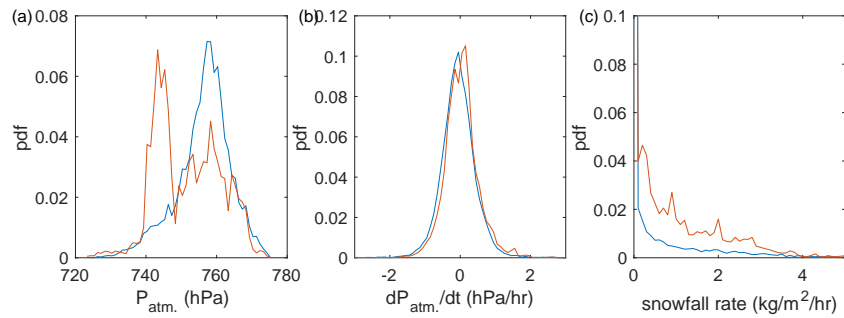


Figure 9. Probability distribution functions (pdf) of the atmospheric pressure (a), hourly atmospheric pressure change (b), and snowfall rate (c). In each plot, the blue curve represents the pdf at all times during seismic acquisition, while the red curves shows the pdf at the times of LFIs. LFIs occur predominantly during low atmospheric pressure (a), increasing atmospheric pressure (b) and during snowfalls (c).

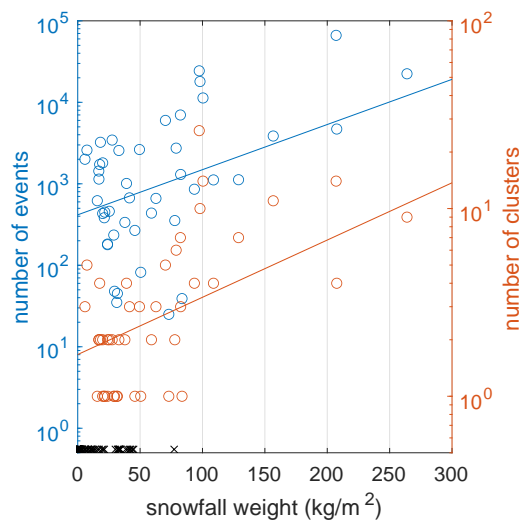


Figure 10. Evolution of the number of events (in blue) and of the number of activated clusters (in red) as a function of the snowfall weight during each snow-fall episode. Black crosses at the bottom indicate snowfall episodes that did not trigger any event.

464

5.4 Icequakes Location and Magnitudes

465

466

467

468

469

470

471

472

473

I have selected all 96 clusters with at least 7 phases picked by at least 4 stations, including at least one station outside Argentière Glacier. These criteria yield a horizontal location accuracy of about 1 km or less. A map is shown in Figure 11. Clusters are located all over the Mont-Blanc massif, from Glacier de Tré la Tête toward the South to Aiguille d'Argentière toward the North. Most clusters are located on or close to glaciers. For clusters outside glaciers, the distance to the closest glacier is generally smaller than the horizontal location accuracy. Figure 11 shows horizontal error ellipses corresponding to the 68% confidence interval, the length of these ellipses should be multiplied by 1.62 to get the 95% confidence intervals.

474

475

476

477

478

479

480

481

482

483

484

Many clusters are located close to the crest between Aiguille des Grand Montets (near station N13) toward the West and Aiguille du Triolet toward the East. The high density of clusters in this area is likely a consequence of the distribution of seismic stations. Indeed, most seismic stations used for the detection (B01, B02 and B03) or the location (N13, N21, N31 and B04) are located on or close to Argentière glacier. Station BLANC was only used for the period 2019/6/14-2022/6/1 and is much noisier than stations B01, B02 and B03. Two clusters detected using station B03 as reference are located far away from Argentière Glacier, one cluster on the eastern face of Mont-Blanc and another cluster below the North face of Grandes Jorasses. The cluster located near the summit of Mont-Blanc has the largest magnitude and the best location accuracy. It was detected by 19 seismic stations up to 68 km away.

485

486

487

488

489

490

491

492

493

494

495

496

497

498

499

500

I also detected one cluster of LFIs located near Glacier de Trèlaporte (longitude 6.931°E, latitude 45.9054°N) and another below Glacier de l'Envers de Blaitière (6.928°E, 45.889°N) with unusual characteristics compared to the other clusters in the Mont-Blanc area. The cluster near Glacier de Trèlaporte is less regular than the other clusters and had a longer typical recurrence time (median of 33 mn). Both clusters were located near 2400 m a.s.l. about 100 m below the front of the glaciers and occurred mainly in late spring and summer. Given the location accuracy, they could possibly occur on the glaciers, which are likely temperate at this elevation. Or they could be associated with gravitational instabilities in the rock induced by the recent glacial retreat in this zone and promoted by the increase in melt-water in spring and summer. Indeed, repeating events have also been detected on landslides (*Uchida and Bürgmann, 2019*). Similar low-frequency repeating signals have been detected on Moosfluh rockslide in Switzerland, a rockslide recently reactivated by the retreat of Aletsch Glacier (*Helmstetter et al., 2018*). This suggests that there is not a single mechanism that explains all our observations, but that different physical processes may generate LFIs, likely different for temperate and cold-based glaciers. And that some of our "LFIs" may in fact be due to landslides.

501

502

503

504

505

506

507

508

509

510

511

512

513

514

515

516

Figure 12 illustrates the characteristics of all located clusters. Most events are shallower than 100 m. Icequake depths range between the surface and 3664 m below, with an average of 746 m and a median of 107 m. Depth is generally smaller than vertical location error, with an average vertical error of 987 m (68% confidence interval). Icequake locations and depths are thus consistent with glacier basal sliding but the large vertical location error does not allow to demonstrate this assumption and to exclude that LFIs could occur within the glacier. Epicenters are often above 3000 m a.s.l, with an average value of 3215 m. The average time residual is 0.14 s, comparable to values obtained for local earthquakes detected by Sismalp in the Mont-Blanc massif. This suggests that both the velocity model and the phase arrivals are correct. The local and surface magnitudes have very similar values ranging between -1.4 and 0.1. A linear fit gives $M_l = 0.85M_s + 0.02$ with a correlation coefficient of 0.93. The surface-waves magnitude M_s better explains the observed amplitudes, probably because seismic signals are dominated by surface waves. The average standard deviation of magnitudes between stations is 0.26 for M_s and 0.29 for M_l . The distribution of magnitudes is difficult to interpret due to the small number of clusters. The decay for $M < -1$ is likely due to the detection thresh-

517 old and to the temporal changes in detection capacity when using different stations for
518 detection.

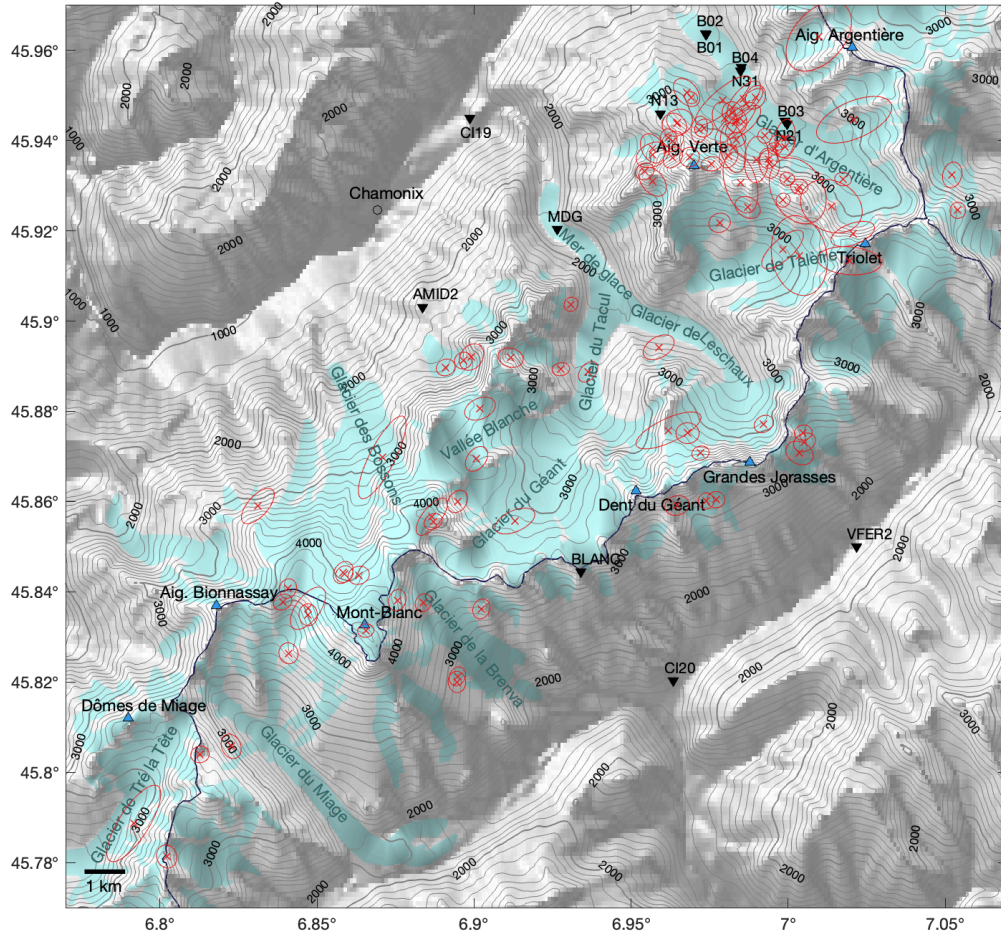


Figure 11. Map of repeating LFIs located in the Mont-Blanc massif (red crosses). Red lines show the horizontal error ellipses at the 68% confidence level. Seismic stations are shown by black triangles. Grey lines show the topography, black lines are national boundaries and blue areas are glaciers.

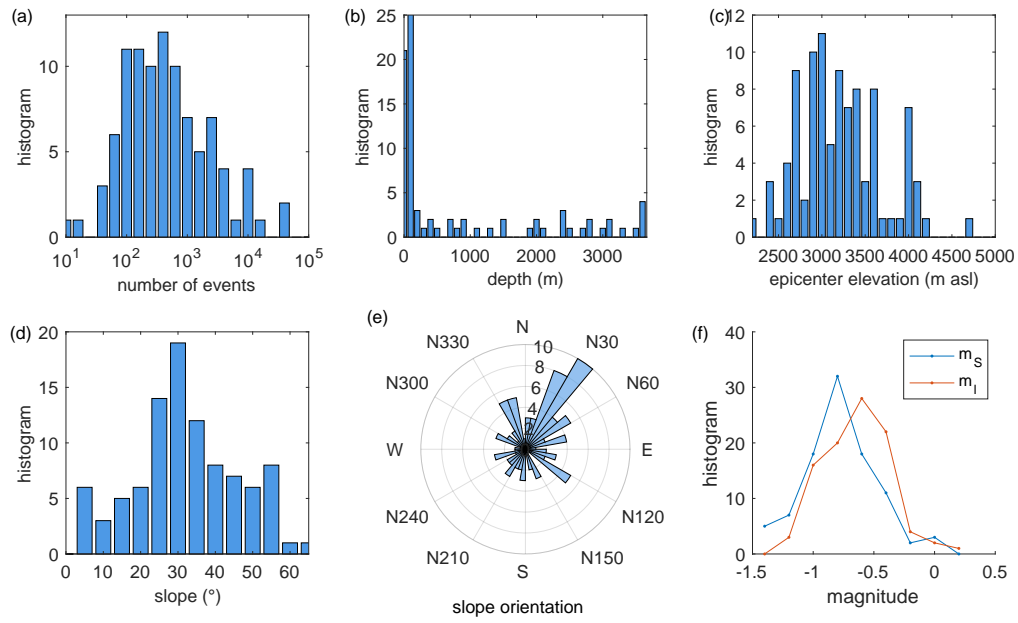


Figure 12. Characteristics of all located clusters: (a) distribution of the number of events per cluster (after removing temporally isolated events), (b) depth, (c) epicentral elevation, (d) slope and (e) slope orientation at the epicenter location, (f) surface wave and local magnitudes of the largest event of each cluster.

Figure 13 shows the seismograms and spectrums for the cluster located near the Mont-Blanc summit. The signal, stacked over all 446 events, is visible as far as 68 km away. The magnitude of the largest event is $M_S = 0$. The signal has the same frequency content over all stations with a peak near 5 Hz. This further suggests that this peak is a source property and is not affected by attenuation.

5.5 Precursory Tremor-Like Signal

While most clusters start with small events and random occurrence times, one cluster initiated on 2021/1/13 as a large amplitude and long-duration signal. This cluster was located near Glacier de la Brenva (6.902°E, 45.836°N) with the epicenter at 3250 m a.s.l. The signal during the first 1000 s of this cluster is shown in Figure 14. The sequence started as a low-frequency but broadband signal (1-15 Hz) that lasted for about 100 s. It was detected at four seismic stations (BLANC, CI20, MFERR and CI19). Because there is no visible P and S waves, it cannot be located accurately. Fixing the hypocenter at the location of the LFI cluster, the regional seismic network Sismalp provides an estimate of the magnitude $m_l = 0.1$. Two LFIs are detected at the beginning of this "tremor", with amplitudes larger than the following events. This suggests that this signal could be a swarm of overlapping LFIs, similar to non-volcanic tremor (*Shelly et al.*, 2006; *Shelly et al.*, 2007). But the "tremor" signal duration and frequency content is also similar to signals generated by snow avalanches, rockfalls or seracs falls. It could also be generated by water flow but this seems unlikely since it occurred in January above 3000 m a.s.l.

5.6 Temporal Changes in Waveforms

Many clusters show progressive changes in waveforms, as illustrated in Figure 15 for the cluster with the largest number of events. This cluster located near the summit of Aiguille Verte was almost continuously active between 2017/12/11 and 2018/1/18. During this period I detected 28978 events at station B01 located at 3.5 km from the source. This cluster is also shown in Figures 1, 2 and 3. I applied a SVD-based Wiener filter to denoise the data (*Moreau et al.*, 2017), keeping the first 15 singular values and the closest 3 neighbors in both time and event index. The first arrivals (P and S waves) show little variation with time, suggesting that the source did not migrate. Apparent variations of S-P arrival times could be due to uncertainties on P-wave picks. I see however clear progressive changes for late arrivals, as large as 0.3 s.

6 Discussion

6.1 Location and Basal Conditions

Most clusters are located on or near glaciers, and at depths shallower than 100 m. Icequake locations and depths are thus consistent with glacier basal sliding. I assume that most LFIs are located at the ice-bed interface but the vertical location accuracy is too large to test this assumption. All repeating icequakes or earthquakes have been located on major shear zones (ice-bed interface, major tectonic faults or subductions zones) (*Podolskiy and Walter*, 2016; *Uchida and Bürgmann*, 2019). The stick-slip phenomena is the only physical process that has been proposed to explain repeating events, except on volcanoes, therefore it seems unlikely that LFIs could be located within the glacier. Focal mechanisms could be used to estimate the source mechanism (e.g., fracture opening or slip, fault plane geometry and slip direction), but because LFI signals are monochromatic and emergent, it is very delicate to identify the direction of P waves first arrivals.

Epicenters are often above 3000 m a.s.l and mainly on North facing slopes (Figures 11 and 12). At these locations, the presence of cold ice is possible. Indeed, a temperature of -2°C has been measured at the base of Tête Rousse glacier, at 3100 m a.s.l.

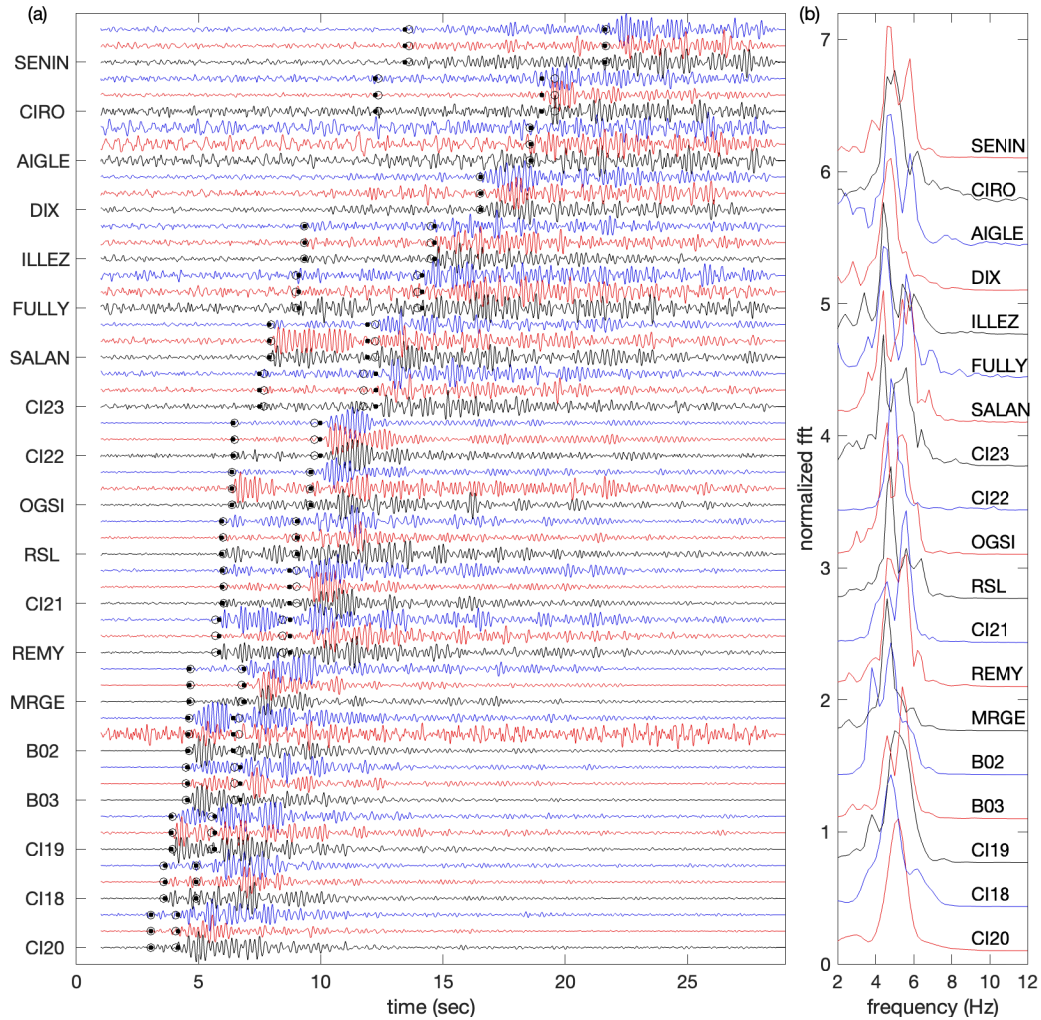


Figure 13. Seismograms (a) and (b) spectrums at all stations where the icequake signal could be picked for the cluster located near the Mont-Blanc summit. Seismograms (ground velocity) were stacked over all events of the cluster, filtered between 2 and 20 Hz and normalized by the peak amplitude of each trace. Picks of P and S waves are shown as black dots and estimated arrival times as open circles. Stations are ordered according to their epicentral distance, from 9 km for station CI20 up to 68 km for station SENIN. Spectrums of the vertical traces in (b) were also normalized by the peak value and shifted vertically for clarity.

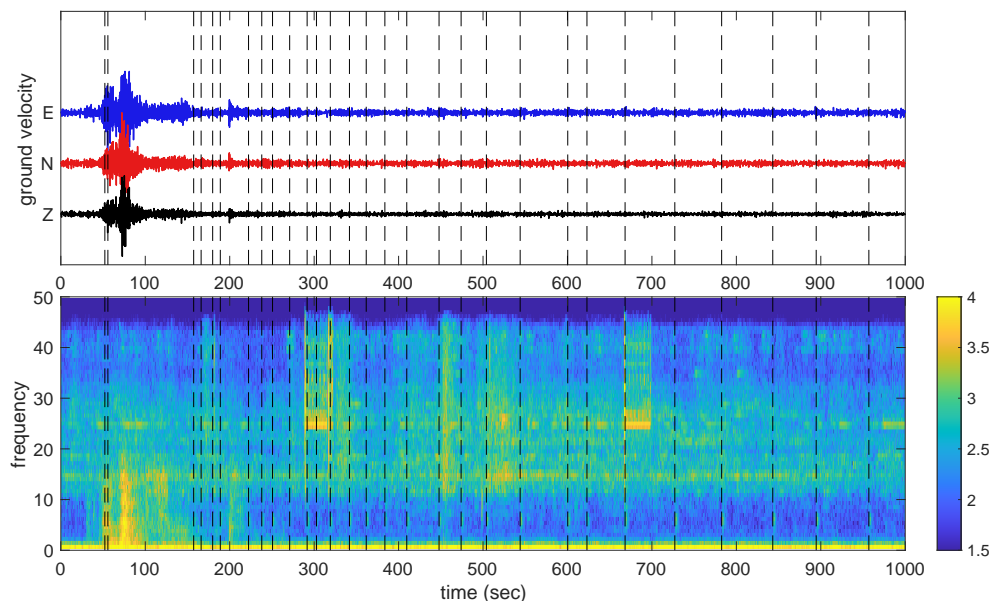


Figure 14. Seismograms (a) and (b) spectrogram of the signal recorded at station BLANC on 2021/1/13 at 21:55 UTC. Black vertical dashed lines correspond to LFIs. This cluster started at 21:55:52 and lasted for 15.78 hours. Seismograms in (a) are bandpass filtered between 1 and 10 Hz. A "tremor-like" signal is visible between about 50 s and 150 s and contains two LFIs. Spectrogram in (b) is averaged over the three components and color represents the \log_{10} of the power spectrum.

567 (*Gilbert et al.*, 2012). Some clusters are clearly associated with cold ice, near Mont-Blanc
 568 summit or Col du Dôme. *Vincent et al.* (2020) measured a temperature of the ice close
 569 to the bedrock of -11°C at Col du Dôme in 2017 (elevation 4250 m a.s.l., latitude 45.841°N ,
 570 longitude 6.8479°E). Many clusters are located around 3000 m a.s.l., possibly close to
 571 the transition between temperate and cold ice.

572 The motion of temperate glaciers (ice-bed interface at the melting point) is mainly
 573 due to basal slip, while cold-based glaciers (ice-bed interface below freezing)
 574 are thought to deform mainly by viscous flow in the bulk of the glacier (*Cuffey and*
 575 *Paterson*, 2010). There are however some observations of basal slip in polar glaciers at
 576 very cold temperatures (*Cuffey et al.*, 1999; *Cuffey and Paterson*, 2010). Laboratory ice-
 577 on-rock or ice-on-till friction experiments have been used to infer how the frictional prop-
 578 erties of ice depend on temperature. These experiments have shown a transition from
 579 a rate-weakening (friction decreasing with sliding velocity) to a rate-strengthening be-
 580 havior for increasing temperatures and a decrease of both healing and friction with tem-
 581 perature (*McCarthy et al.*, 2017; *Zoet et al.*, 2018). A rate-weakening behavior is required
 582 to generate dynamic rupture such as earthquakes or icequakes. The transition to rate-
 583 weakening friction is also favored by increasing sliding velocity, increasing debris con-
 584 centration, and increasing drainage (*McCarthy et al.*, 2017; *Zoet et al.*, 2018). Other stud-
 585 ies suggested that stick-slip events at the base of temperate glaciers or ice-streams could
 586 be due to the friction of sediments entrained by the glacier motion (*Lipovsky et al.*, 2019)
 587 or to the ploughing of clasts embedded in the base of the ice through till (*Barcheck et*
 588 *al.*, 2018; *Thomason and Iverson*, 2008). So far, laboratory friction experiments with ice-
 589 rock or ice-till interfaces have only observed a velocity-weakening behavior for cold ice,
 590 even for debris-laden ice (*McCarthy et al.*, 2017; *Saltiel et al.*, 2021; *Zoet et al.*, 2018).

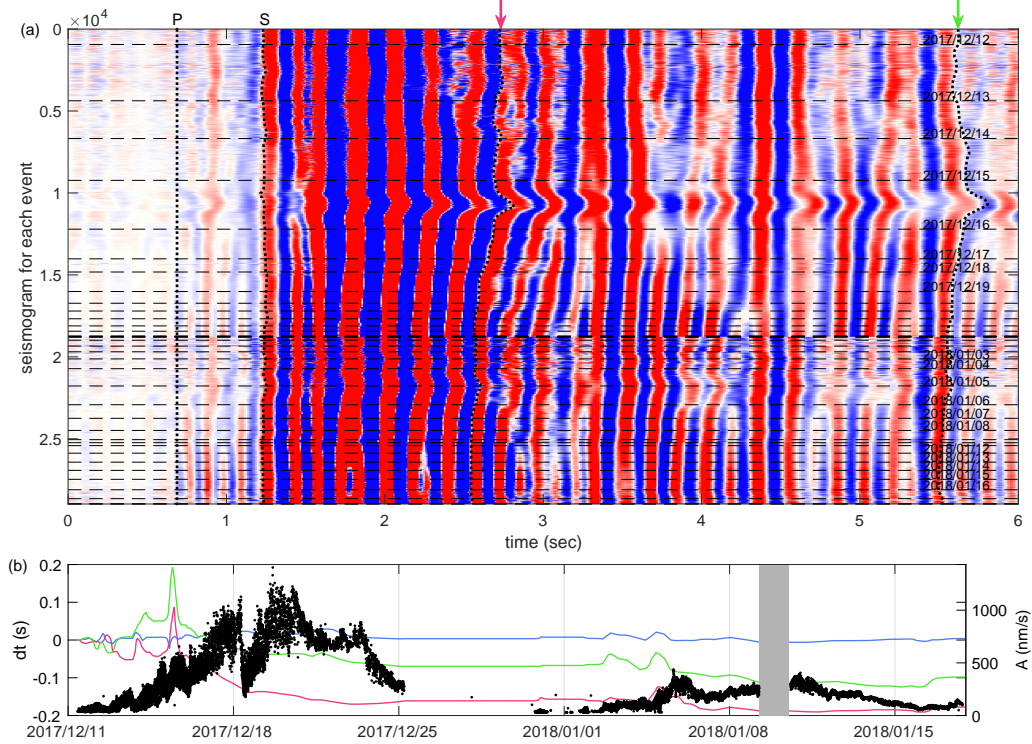


Figure 15. Temporal changes in waveforms for a cluster detected at station B01. (a) Seismograms for the North component of station B01 filtered between 2 and 20 Hz and normalized by the peak amplitude of each trace. I also applied a SVD-based Wiener filter (*Moreau et al., 2017*) to improve the signal-to-noise ratio. Seismograms are aligned on the P wave arrival time, which was manually picked on the vertical channel with a stronger P wave amplitude than the north component. Arrival times of P and S waves are shown as near-vertical dotted lines (manual picks). The other two dotted lines marked by arrows correspond to late phase arrivals with strong temporal variations. Each dashed horizontal line corresponds to a new day. (b) Arrival time of different phases relative to the P wave arrival time and relative to the first event of the cluster: blue line for the S wave, pink and green lines for each phase indicated by a pink and green arrow respectively in (a). Black dots show the peak amplitude of each event. The grey area indicates a data gap.

591 Much larger and lower frequencies icequakes repeat about twice a day at the base
 592 of Willans Ice Stream in Antarctica because basal friction is modulated by oceanic tides
 593 (*Wiens et al.*, 2008). While most of the ice-stream is temperate at the base, the recent
 594 slowdown of the ice-stream and the occurrence of repeating stick-slip events may be due
 595 to basal freezing, with stick-slip events occurring on islands of cold based ice (*Joughin*
 596 *et al.*, 2004; *Saltiel et al.*, 2021).

597 6.2 Source properties

598 From the magnitudes of LFIs, we can estimate possible values of source properties.
 599 The seismic moment M_0 is related to the moment magnitude M_w by $M_w = \log_{10}(M_0)/1.5 - 6.03$
 600 (*Hanks and Kanamori*, 1979). Assuming that our values of $-1.4 < M_s < 0$ are rep-
 601 resentative of M_w , I obtain a seismic moment ranging between 8.9×10^6 and 1.1×10^9
 602 N.m for the largest event of each cluster. These values are much larger than the moment
 603 magnitude $-3.2 < M_w < -2.2$ estimated for the high frequency icequakes detected
 604 at Argentière glacier (*Helmstetter et al.*, 2015). The seismic moment is related to the shear
 605 modulus μ (2.3 GPa for ice), the slip d and the rupture area A by $M_0 = \mu Ad$. I can
 606 thus only constrain the product of rupture area and slip. I can get a lower bound on the
 607 rupture radius $r = \sqrt{A/\pi}$ by assuming that during bursts of LFIs all the glacier dis-
 608 placement is due to seismic slip. This assumption may overestimate the seismic slip (and
 609 underestimate rupture length) if there is significant viscous deformation or underesti-
 610 mate d and over-estimate r if there is an acceleration of glacier displacement during bursts
 611 of LFIs. Cold glaciers move much slower than temperate glaciers. *Vincent et al.* (2020)
 612 measured a maximum ice flow velocity of 10 m/yr at Col du Dôme in 2017. The clus-
 613 ter with the largest magnitude $M_s = 0$ (located near the summit of Mont-Blanc) has
 614 a median recurrence time of 1000 s. This gives a slip per event of 0.3 mm and a rupture
 615 length of 23 m. If only half of the displacement is due to basal slip, then the slip is 0.15
 616 mm and the rupture length $r = 33$ m.

617 The stress drop $\Delta\tau$ can be estimated as

$$\Delta\tau = \mu \frac{d}{r} \frac{7\pi}{16} \quad (4)$$

618 for a circular rupture (*Eshelby*, 1957), yielding $\Delta\tau = 42$ kPa for $d = 0.3$ mm and a
 619 radius $r = 23$ m. This value is about one hundred times smaller than the value observed
 620 for tectonic earthquakes (*Abercrombie*, 1995). It is about 100 times larger than the nor-
 621 mal stress induced by the smallest snowfalls that trigger LFIs.

622 We can also estimate the rupture length from the main frequency of the signal, as-
 623 suming that the peak in the spectrum corresponds to the corner frequency. *Madariaga*
 624 (1976) derived the following relation between the rupture radius r and the corner fre-
 625 quency f_c

$$f_c = kV_S/r \quad (5)$$

626 for numerical 2D simulations of a circular crack expanding at a constant rupture veloc-
 627 ity V_r . Assuming $V_r = 0.9V_S$, the constant k is equal to 0.21 for shear waves. Assum-
 628 ing $f_c = 5$ Hz and a shear wave velocity $V_S = 2500$ m/s (intermediate between the
 629 value in the ice and in the bedrock) I obtain a source radius $r = 105$ m. This value is
 630 comparable with but larger than the length $r = 23$ m estimated above from the max-
 631 imum seismic moment and the glacier velocity. This suggests that LFIs only account for
 632 a small fraction of glacier displacement rate even during bursts of LFIs. Using this value
 633 of the source radius $r = 105$ m and a maximum seismic moment of 1.1×10^9 , I obtain
 634 a slip of 14 μm and a stress drop of 0.4 kPa comparable with the stress change induced
 635 by snowfalls.

636

6.3 Temporal changes in waveforms

637

638

639

640

641

642

643

644

645

646

647

648

649

650

Many clusters of repeating LFIs show progressive changes in waveforms, as illustrated in Figure 15. Figure 15a shows the waveforms of a cluster of 28000 LFIs that occurred near the summit of Aiguille Verte about 3.5 km away from station B01. Arrival times in the coda of both P and S waves vary by up to 0.2 s while the first arrivals do not change (Figure 15b). This suggests that the nucleation point does not evolve during clusters, i.e, there is no evidence for migration in time. These variations could thus be explained by changes in the medium, by changes in the rupture area or in the rupture velocity. I don't think that changes in the medium could explain such large changes in travel times (up to 10%) over such short time periods (a few hours or days). Most of these clusters occur in winter at large elevations where there is no or very little water. The snow layer evolves with time but the low-frequency seismic waves near 5 Hz are not strongly sensitive to this shallow layer. I thus propose two explanations for these changes in seismic signals, either changes in the rupture area or changes in the rupture velocity. Both parameters control the rupture duration and the signal frequency content.

651

652

653

654

655

656

657

658

659

660

A very slow rupture velocity of about 150 m/s has been measured for repeating basal icequakes at Whillans Ice Stream in West Antarctica (*Wiens et al., 2008*). *Walter et al. (2011)* further observed temporal changes in rupture velocity between 100 and 300 m/s between successive events, correlated with inter-event times and slip amount. *Walter et al (2015)* reproduced these results in a laboratory stick-slip experiment, showing that rupture velocity depends on pre-rupture stress. A progressive change in rupture velocity could explain our observations of changes in seismic waveforms. However, in our case I found no clear correlation between changes in seismic waveform and changes in the amplitude of repeating LFIs (see Figure 15b). I thus don't know how to explain these possible changes in rupture velocity or rupture length.

661

662

663

664

665

666

It is not clear whether the duration of the signal larger than 5s is due to the source or to the seismic waves propagation. If the rupture lasts for several seconds, it suggests a very slow rupture to be consistent with the rupture length $r = 105$ m estimated from the main frequency of the signal of 5 Hz. Because of the shallow source, of the heterogeneous medium and of the complex topography, it is possible that the late arrivals are diffracted or reflected waves rather than direct waves.

667

6.4 Triggering by snow

668

669

670

671

672

673

674

675

676

677

678

679

Repeating LFIs are mainly observed during and after snowfalls, while high-frequency icequakes are not sensitive to snowfalls (*Helmstetter et al., 2015*). Our observations are very similar to LFIs detected at Mount Rainier, an ice-covered volcano in the USA (*Allstadt and Malone, 2014; Thelen et al., 2013*). Both sites generate bursts of LFIs lasting for days or weeks and triggered by snowfalls, with similar recurrence times of a few minutes, magnitudes $-1 < M < 0$ and peak frequency around 5 Hz. *Allstadt and Malone (2014)* reported that Mount Rainier is a temperate glacier, whose displacement is dominated by basal sliding, and interpreted the LFIs at Mount Rainier as due to stick-slip on asperities surrounded by aseismic basal sliding. However, the location of icequakes at Mount Rainier is not well constrained, and they could be located near the top of the volcano (at 4392 m a.s.l.) where the ice temperature is likely below the melting point (*Mills, 1979*).

680

681

682

683

684

685

Allstadt and Malone (2014) also observed a progressive change in waveforms within each cluster using coda wave interferometry, which they interpreted as due to a migration of the source with the glacier flow. In our case, I interpreted the temporal change in seismic waveforms as due to variations of rupture length and/or rupture velocity, because the first P and S arrivals did not change. This assumption may also explain the variations in seismic waveforms at Mount-Rainier.

686 *Allstadt and Malone* (2014) suggested that additional loading due to snowfalls per-
 687 turbs the glaciers from smooth sliding to stick-slip regime. Using a rate-and-state fric-
 688 tion law (*Dieterich, 1979*) to model the sliding of the glacier over its bed, we can indeed
 689 reproduce a transition from stable sliding to the stick-slip regime by increasing normal
 690 stress (*Helmstetter et al., 2018; Lipovsky et al., 2017*). The increase in normal stress as-
 691 sociated with snowfalls is however partly cancelled by the associated decrease in atmo-
 692 spheric pressure, but the overall effect of atmospheric pressure and snow weight tends
 693 to increase the normal stress toward the end of each snowfall episode, when most LFIs
 694 occur (Figure 8).

695 The change in normal stress associated with snowfalls is very small compared with
 696 the normal stress at the base of glaciers. A snowfall of 25 cm with a density of 0.4 in-
 697 creases the normal stress by about 1 kPa, about 0.1% of the normal stress at the base
 698 of a 100 m thick glacier. It is thus surprising that such a small stress change triggers so
 699 many LFIs. However, earthquakes have been shown to be even more sensitive to smaller
 700 relative stress perturbations. Seismicity is modulated by ocean tides, corresponding to
 701 a stress change of about 10 kPa, while the normal stress at 10 km depth is about 300 MPa
 702 (*Thomas et al., 2009*). This high susceptibility of earthquakes and LFIs suggests that
 703 faults and ice-bed interfaces are very close to the rupture threshold, at least at some points,
 704 and that rupture initiates rapidly when stress reaches the failure threshold.

705 For Alpine glaciers very close to the melting point temperature, another mecha-
 706 nism could explain the triggering by snowfalls. The additional weight induced by snow-
 707 falls slightly decreases the melting point temperature, so that the basal temperature may
 708 reach the melting point temperature. This could produce a transition between a locked
 709 ice-bed interface for cold ice and stable sliding at the melting point, which could be as-
 710 sociated with stick-slip events progressively leading to stable sliding. The increase in pres-
 711 sure due to a typical snowfall of 25 cm with a density of 0.4 is about 1 kPa, leading to
 712 a change in melting temperature of about 10^{-4} K (Clausius-Clapeyron constant). There-
 713 fore this mechanism may only be active very close to the transition between cold-based
 714 and temperate glaciers.

715 The correlation between snowfalls and LFIs could suggest that LFIs occur within
 716 or at the base of the fresh snow layer. But then it is difficult to explain why LFIs oc-
 717 cur regularly in time and why they mainly occur above 3000 m a.s.l. And because seis-
 718 mic waves attenuate very fast in the snow and shear modulus is much smaller in the snow
 719 than in the ice, it is difficult to explain how the signal could be detected up to 68 km
 720 away.

721 Repeating LFIs triggered by snow falls have also been detected on Gugla rock glacier
 722 in Switzerland (46.1394°N, 7.8183°E) (*Guillemot et al., 2020; Helmstetter et al., 2018*).
 723 These studies suggested that these events were associated with stick-slip behavior at the
 724 base of the rock-glacier. However, I realized that most clusters detected at Gugla were
 725 also visible at other permanent seismic stations (stations MMK, SIMPL, EMBD, SNIB,
 726 VANNI and DIX in Switzerland, network code CH and Italian station SATI, network
 727 code GU). Several clusters have been located at distances between 2 and 7 km East or
 728 South-East from Gugla. These locations are not very accurate but are all possibly as-
 729 sociated with glaciers above 3000 m a.s.l. These events are thus very similar to LFIs in
 730 the Mont-Blanc area and may be produced by the same physical processes.

731 **6.5 Comparison with earthquakes**

732 Both faults and subglacial slip exhibit a wide spectrum of behavior, from stable
 733 slow slip to dynamic rupture, with transient slip events ranging over a wide range of spa-
 734 tial and temporal scales (*Peng and Gomberg, 2010*). Tectonic faults and subduction zones
 735 produce both fast earthquakes, with duration of the order of seconds, and slow slip events,
 736 with duration of days or months, and probably a continuum of slip modes in between

737 (*Thøgersen et al.*, 2019). LFIs in the Mont-Blanc area share several properties with low-
 738 frequency earthquakes (LFEs). LFEs are due to shear slip on faults like regular earth-
 739 quakes but their signal lack of high frequency energy. They are mainly detected on trans-
 740 form faults (e.g. San Andreas) or subduction zones in the lower part of the locked seis-
 741 mogenic zone near the brittle-ductile transition (*Shelly et al.*, 2006; *Shelly et al.*, 2007).
 742 LFEs have much smaller stress drops, smaller slip-rates and smaller rupture velocities
 743 than regular earthquakes (*Thomas et al.*, 2016). Like LFIs, LFEs can be triggered by
 744 very small perturbations, like distant earthquakes or tides. *Thomas et al.* (2009) observed
 745 that LFEs on the San Andreas are very sensitive to tidally induced shear stress changes
 746 with peak-to-peak amplitudes less than 0.5 kPa. Both LFEs and LFIs seem to occur mainly
 747 near the transition between stable sliding (under temperate glaciers for LFIs and below
 748 the seismogenic zone for LFEs) and locked areas (under cold-based glaciers for LFIs and
 749 in the seismogenic zone for LFEs). LFEs are more sensitive than regular earthquakes
 750 to small stress changes. Similarly, the small snowfalls that trigger LFIs in the Mont-Blanc
 751 area do not produce any increase in the rate of HFIs (*Helmstetter et al.*, 2015).

752 Repeating earthquakes occur regularly on the same asperity (*Nadeau et al.*, 1995;
 753 *Uchida and Bürgmann*, 2019). The stress increases between events due to aseismic slip
 754 around the asperity. This mechanism can also explain the repeating HFIs on temper-
 755 ate glaciers, which have a large amount of aseismic basal slip. However, many LFIs oc-
 756 cur on cold-based glaciers, so that there is very little slip at the ice-bed interface. The
 757 reloading between stick-slip events may thus be due to viscous creep within the bulk of
 758 the glacier rather than from slip around the asperity.

759 **7 Conclusion and Perspectives**

760 I have discovered repeating LFIs in the Mont-Blanc massif. Some clusters of LFIs
 761 are located on cold based glaciers (e.g., near Mont-Blanc summit or near Col du Dôme),
 762 a few ones on temperate glaciers or possibly on rockslides activated by glacial unload-
 763 ing. For most clusters the basal conditions are unknown but are likely close to the melt-
 764 ing point temperature.

765 I found both similarities and major differences between repeating HFIS and LFIs
 766 Both LFIs and HFIs occur more or less regularly in time, repeating every few minutes,
 767 and display progressive changes in amplitude and recurrence times. While HFIs are lo-
 768 cated at the base of temperate alpine glaciers, most LFIs are located at higher elevations.
 769 LFIs are triggered by snowfalls while HFIs are not sensitive to snowfalls. The differences
 770 between HFIs and LFIs are similar to the ones between regular earthquakes and LFEs,
 771 suggesting that they reflect common physical processes controlling rupture nucleation
 772 and propagation. Low-frequency events are more sensitive to smaller perturbations, oc-
 773 cur near the transition between the locked and the creeping areas, and have slower rup-
 774 ture velocities and smaller stress drop compared with high-frequency events. Understand-
 775 ing what controls the nucleation of LFIs could yield important information on basal prop-
 776 erties and their temporal evolution.

777 The sources properties (depth, rupture length, rupture velocity, stress drop) of LFIs
 778 are difficult to estimate because I do not have near-field data. LFIs are difficult to mon-
 779 itor because they occur mainly at high elevations, on steep faces exposed to snow avalanches
 780 or serac falls. Installing seismometers in such places is thus difficult and dangerous. In
 781 addition, bursts of LFIs usually last for a few days and mainly occur during snowfalls.
 782 Even if we can detect and locate in real time the beginning of a cluster, we cannot go
 783 in the field to install seismometers nearby when the weather is bad, and LFIs often stop
 784 before the weather improves. Satellite images could be used remotely and retrospectively
 785 to estimate glacier motion. They could be used to test whether the glacier accelerates dur-
 786 ing bursts of LFIs or if clusters of LFIs occur at constant displacement rate. LFIs could
 787 be due to a transition between creep-dominated deformation within the glacier and basal

788 stick-slip motion. However, while some studies have estimated the average displacement
 789 rate in the Mont-Blanc area, the resolution is not yet good enough to detect short-term
 790 (days to weeks) temporary variations in velocity (*Millan, 2019*).

791 Similar repeating LFIs have also been observed in the Swiss Alps (*Helmstetter et*
 792 *al., 2018*) and at Mount Rainier (*Allstadt and Malone, 2014*). They probably occur else-
 793 where on Alpine glaciers. Trying to detect these events using existing regional seismic
 794 networks near glaciated areas could help us to understand the link between LFIs and glacier
 795 basal conditions.

796 Numerical modeling could be interesting to learn more about LFIs source processes
 797 and triggering mechanisms. We could try to simulate seismic signals of LFIs by chang-
 798 ing the rupture velocity or the rupture length to reproduce the observed temporal changes
 799 in seismic waveforms. Several processes could explain the triggering of LFIs by snow-
 800 fall, either due to the increase in normal and shear stress or due the tiny change in melt-
 801 ing point temperature with pressure. Numerical simulations could be used to test both
 802 hypothesis. *Helmstetter et al. (2018)* already attempted to reproduce repeating LFIs us-
 803 ing the rate-and-state friction law. However, they assumed aseismic basal slip around
 804 the asperity. Our observations suggest that most LFIs occur on cold-based glacier, so
 805 that deformation is dominated by viscous creep rather than by basal slip. We could also
 806 test different friction laws developed for basal sliding, such as the model of *Gagliardini*
 807 *et al. (2007)*.

808 8 Data availability statement

809 Some seismological data are available from the Federation of Digital Seismograph
 810 Networks (FDSN) network with network codes CH, GU, IV, FR, ZO, 1D, 8C. The list
 811 of all seismic stations used and network codes are given in Table 1. Some data is distributed
 812 by FDSN with restricted access (network codes XT, 8D). Data from temporary stations
 813 B01-B04, DOM and MDG on glaciers in the massif are (not yet) open and I am not al-
 814 lowed to share them. Catalogs of repeating LFIs and cluster locations are provided at
 815 <https://doi.org/10.5281/zenodo.6822165>. Meteorological data is available from GLACIO-
 816 CLIM observatory (*Vincent et al., 2009*) and S2M database (*Vernay et al., 2019*). We
 817 used nonlinloc software (*Lomax et al., 2000*) to locate LFIs. This program can be down-
 818 loaded from <http://alomax.free.fr/nllloc/> and my input files (station locations, ar-
 819 rival times, velocity models, topography) can be downloaded from [https://doi.org/](https://doi.org/10.5281/zenodo.6822165)
 820 [10.5281/zenodo.6822165](https://doi.org/10.5281/zenodo.6822165).

821 Acknowledgments

822 I thank Florent Gimbert and Ugo Nanni for sharing their seismic data (stations B01-
 823 B04, DOM and MDG) and Toni Kraft for providing data of stations MFERR, VFER2
 824 and AMID2. I thank Benoit Urruty, Laurent Ott and others for their help in the field.
 825 Some instruments (nodes N11-N35, new stations CI18-CI20) belong to the French Na-
 826 tional Pool of Portable Seismic Instruments (Sismob-RESIF). I thank Michel Bouchon,
 827 Florent Gimbert, Ugo Nanni, James Hollingsworth, Emmanuel Chaljub, Mathieu Causse,
 828 Luc Moreau and Roland Bürgmann for interesting discussions. This work was supported
 829 by the SAUSSURE project (<https://saussure.osug.fr>) (ANR-18-CE01-0015) funded by
 830 the Agence National de la Recherche (ANR). ISTerre is part of Labex OSUG@2020 (ANR10
 831 LABX56).

832 References

833 Abercrombie RE (1995). Earthquake source scaling relationships from -1 to 5 M_L
 834 using seismograms recorded at 2.5-km depth. *J. Geophys. Res.*, 100, 24015-
 835 24036.

- 836 Allen R.V. (1978). Automatic earthquake recognition and timing from single traces,
837 *Bull. seism. Soc. Am.* 68, 1521-1532
- 838 Allstadt, K., and S. D. Malone (2014). Swarms of repeating stick-slip icequakes trig-
839 gered by snow loading at Mount Rainier volcano, *J. Geophys. Res. Earth Surf.*,
840 119, 1180–1203, doi:10.1002/2014JF003086.
- 841 Barcheck, C. G., S. Tulaczyk, S. Y. Schwartz, J. I. Walter, and J. P. Winberry
842 (2018). Implications of basal micro-earthquakes and tremor for ice stream me-
843 chanics: Stick-slip basal sliding and till erosion, *Earth Planet. Sci. Lett.* 486,
844 54–60, doi:10.1016/j.epsl.2017.12.046.
- 845 Bormann, P., and J. W. Dewey (2014). The new IASPEI standards for determin-
846 ing magnitudes from digital data and their relation to classical magnitudes,
847 In: Bormann, P. (Ed.), *New Manual of Seismological Observatory Practice*
848 2 (NMSOP-2), Potsdam : Deutsches GeoForschungsZentrum GFZ, 1-44,
849 https://doi.org/10.2312/GFZ.NMSOP-2_IS_3.3
- 850 Cuffey, K.M., H. Conway, B., Hallet, A.M., Gades and C.F. Raymond (1999). Inter-
851 facial water in polar glaciers, and glacier sliding at -17°C , *Geophys. Res. Lett.*,
852 26, 751-754, doi:10.1029/1999GL900096.
- 853 Cuffey, K., and W. Paterson (2010). *The Physics of Glaciers*, Elsevier, Butterworth-
854 Heinemann, Burlington, Mass.
- 855 Dieterich, J. H. (1979). Modeling of rock friction, 1. Experimental re-
856 sults and constitutive equations, *J. Geophys. Res.* 84, 2169–2175,
857 doi:10.1029/JB084iB05p02169.
- 858 Eshelby, J. D. (1957), The determination of the elastic field of an ellipsoidal inclu-
859 sion, and related problems, *Proc. R. Soc. A*, 241(1226), 376-396.
- 860 Gagliardini, O., D. Cohen, P. Råback, and T. Zwinger (2007), Finite-element mod-
861 eling of subglacial cavities and related friction law, *J. Geophys. Res.*, 112,
862 F02027, doi:10.1029/2006JF000576.
- 863 Gibbons, S. J., and F. Ringdal (2006). The detection of low magnitude seismic
864 events using array-based waveform correlation, *Geophys. J. Int.*, 165, 149–166.
- 865 Gilbert, A., C. Vincent, P. Wagnon, E. Thibert, and A. Rabatel (2012). The influ-
866 ence of snow cover thickness on the thermal regime of Tête Rousse Glacier
867 (Mont Blanc range, 3200 m a.s.l.): Consequences for outburst flood haz-
868 ards and glacier response to climate change, *J. Geophys. Res.*, 117, F04018,
869 doi:10.1029/2011JF002258.
- 870 Gimbert, F., U. Nanni, P. Roux, A. Helmstetter, S. Garambois, A. Lecointre,
871 A. Walpersdorf, B. Jourdain, M. Langlais, O. Laarman, F. Lindner,
872 A. Sergeant, C. Vincent and F. Walter (2021). A multi-physics experi-
873 ment with a temporary dense seismic array on the Argentière Glacier,
874 french Alps: the RESOLVE project, *Seismol. Res. Lett.* 92(2A), 1185-1201,
875 <https://doi.org/10.1785/0220200280>.
- 876 Guillemot, A., Helmstetter, A., Larose, E., Baillet, L., Garambois, S., Mayoraz, R.,
877 (2020). Seismic monitoring in the Gugla rock glacier (Switzerland): ambient
878 noise correlation, microseismicity and modelling, *Geophys. J. Int.*, 221(3),
879 1719–1735.
- 880 Hanks T. C and H. Kanamori (1979), Moment magnitude scale, *J. Geophys. Res.*,
881 84(B5), 2348-2350.
- 882 Helmstetter, A., B. Nicolas, P. Comon, and M. Gay (2015). Basal icequakes
883 recorded beneath an alpine glacier (Glacier d’Argentière, Mont Blanc,
884 France) : evidence for stick-slip motion? *J. Geophys. Res.* 120(3),
885 doi:10.1002/2014JF003288.
- 886 Helmstetter, A., B. Lipovsky, E. Larose, L. Baillet and R. Mayoraz (2018). Repeat-
887 ing quakes triggered by snow-falls at Gugla rock-glacier : transition between
888 stable slip and stick-slip?, SSA meeting, Miami, 13-17 May 2018, *Seism. Res.*
889 *Lett.* 89(2B)

- 890 Helmstetter, A., E. Larose, L. Baillet and R. Mayoraz (2018). Repeating quakes de-
 891 tected at Moosfluh Rockslide (Valais, Switzerland), SSA meeting, Miami, 13-17
 892 May 2018, *Seism. Res. Lett.* *89(2B)*
- 893 Helmstetter, A. and RESIF (2020). Seismic network 1D: Temporary instal-
 894 lation of 13 sensors (3C fairfield nodes) on Argentière Glacier and near
 895 Col des Grands Motets in the Mont Blanc massif (RESIF-SISMOB)
 896 [Data set]. RESIF - Réseau Sismologique et géodésique Français,
 897 <https://doi.org/10.15778/RESIF.1D2019>
- 898 Helmstetter, A., P. Guéguen and RESIF (2020). Seismic network 8C: mon-
 899 itoring swarms in the Mont-Blanc and Vallorcine area (RESIF - SIS-
 900 MOB) [Data set]. RESIF - Réseau Sismologique et géodésique Français,
 901 <https://doi.org/10.15778/RESIF.8C2019>
- 902 INGV Seismological Data Centre (2006). Rete Sismica Nazionale (RSN). Is-
 903 tituto Nazionale di Geofisica e Vulcanologia (INGV), Italy [Data set].
 904 <https://doi.org/10.13127/SD/X0FXnH7QfY>
- 905 Jarvis, A., E. Guevara, H. I. Reuter, and A. D. Nelson (2008). Hole-filled SRTM for
 906 the globe : version 4 : data grid. Web publication/site, CGIAR Consortium for
 907 Spatial Information. <http://srtm.csi.cgiar.org/>
- 908 Joughin, I., S. Tulaczyk, D. R. MacAyeal, and H. Engelhardt (2004), Melting and
 909 freezing beneath the Ross ice streams, Antarctica, *J. Glaciol.* *50(168)*, 96-108.
- 910 Kufner, S. K., A. M. Brisbourne, A. M. Smith, H. S. Hudson, T. Murray, R.
 911 Schlegel, J. M. Kendall, S. Anandakrishnan, and I. Lee (2021). Not all ice-
 912 quakes are created equal: Basal icequakes suggest diverse bed deformation
 913 mechanisms at Rutford Ice Stream, West Antarctica, *J. Geophys. Res. Earth*
 914 *Surf.*, *126*, e2020JF006001, <https://doi.org/10.1029/2020JF006001>
- 915 Lipovsky, B. P., and E. M. Dunham (2017). Slow-slip events on the Whillans
 916 Ice Plain, Antarctica, described using rate-and-state friction as an
 917 ice stream sliding law, *J. Geophys. Res. Earth Surf.*, *122*, 973–1003,
 918 doi:10.1002/2016JF004183.
- 919 Lipovsky, B. P., C. R. Meyer, L. K. Zoet, C. McCarthy, D. D. Hansen, A. W. Rem-
 920 pel, and F. Gimbert (2019). Glacier sliding, seismicity and sediment entrain-
 921 ment, *Annals of Glaciology*, *60(79)*, 182-192, doi:10.1017/aog.2019.24.
- 922 Lomax, A., J. Virieux, P. Volant and C. Berge (2000). Probabilistic earthquake lo-
 923 cation in 3D and layered models: Introduction of a Metropolis-Gibbs method
 924 and comparison with linear locations, in *Advances in Seismic Event Location*
 925 Thurber, C.H., and N. Rabinowitz (eds.), Kluwer, Amsterdam, 101-134.
- 926 Madariaga, R. (1976). Dynamics of an expanding circular fault, *Bull. seism. Soc.*
 927 *Am.*, *66(3)*, 639-666.
- 928 McCarthy, C., H. Savage, and M. Nettles (2017). Temperature dependence of ice-
 929 on-rock friction at realistic glacier conditions, *Philos. Trans. R. Soc. A* *375*,
 930 20150348.
- 931 Millan R., J. Mouginot, A. Rabatel, S. Jeong, D. Cusicanqui, A. Derkacheva and M.
 932 Chekki (2019). Mapping surface flow velocity of glaciers at regional scale using
 933 a multiple sensors approach, *Remote Sens.*, *11*, 2498, doi:10.3390/rs11212498.
- 934 Mills, H.H. (1979). Some implications of sediment studies for glacial erosion on
 935 Mount Rainier, Washington, *Northwest Science*, *53(3)*, 190-199.
- 936 Moreau, L., L. Stehly, P. Boué, Y. Lu, E. Larose and M. Campillo (2017). Improving
 937 ambient noise correlation functions with an SVD-based Wiener filter *Geophys.*
 938 *J. Int.* *211(1)*, 418–426, doi: 10.1093/gji/ggx306.
- 939 Nadeau, R. M., W. Foxall, and T. V. McEvilly (1995). Clustering and periodic re-
 940 currence of microearthquakes on the San Andreas Fault at Parkfield, Calif.,
 941 *Science*, *267*, 503–507.
- 942 Nanni, U., F. Gimbert, C. Vincent, D. Gräff, F. Walter, L. Piard, and L. Moreau
 943 (2020), Seasonal and Diurnal Dynamics of Subglacial Channels: Obser-
 944 vations Beneath an Alpine Glacier, *The Cryosphere*, *14(5)*, 1475-1496,

- 945 <https://doi.org/10.5194/tc-14-1475-2020>.
- 946 Peng, Z. and J. Gomberg (2010), An integrated perspective of the continuum be-
 947 tween earthquakes and slow-slip phenomena. *Nat. Geosci.* 3, 599-607.
- 948 Podolskiy, E. A., and F. Walter (2016). Cryoseismology, *Rev. Geophys.* 54(4),
 949 2016RG000526, doi:10.1002/2016RG000526.
- 950 RESIF (1995). RESIF-RLBP French Broad-band network, RESIF-RAP
 951 strong motion network and other seismic stations in metropolitan
 952 France [Data set]. RESIF - Réseau Sismologique et géodésique Français,
 953 <https://doi.org/10.15778/RESIF.FR>
- 954 Rössli C., A. Helmstetter, F. Walter, and E. Kissling (2016). Meltwater influences
 955 on deep stick-slip icequakes near the base of the Greenland Ice Sheet, *J. Geo-*
 956 *phys. Res. Earth Surf.* 121(2), 2015JF003601, doi:10.1002/2015JF003601.
- 957 Roux, P., Gimbert, F. and RESIF (2021). Dense nodal seismic array tem-
 958 porary experiment on Alpine Glacier of Argentière (RESIF-SISMOB)
 959 [Data set]. RESIF - Réseau Sismologique et géodésique Français.
 960 <https://doi.org/10.15778/RESIF.ZO2018>
- 961 Salties, S., C. McCarthy, T. T. Creyts and H. M. Savage (2021). Experimental evi-
 962 dence of velocity-weakening friction during ice slip over frozen till: implications
 963 for basal seismicity in fast moving, soft-bed glaciers and ice streams, *Seismol.*
 964 *Res. Lett.* XX, 1-18, doi:10.1785/0220200480.
- 965 Schaff, D. P., and P. G. Richards (2011). On finding and using repeat-
 966 ing seismic events in and near China, *J. Geophys. Res.*, 116, B03309,
 967 doi:10.1029/2010JB007895.
- 968 Shelly, D. R., G. C. Beroza, S. Ide, and S. Nakamura (2006). Low-frequency earth-
 969 quakes in Shikoku, Japan, and their relationship to episodic tremor and slip,
 970 *Nature*, 442, 188–191, doi:10.1038/nature04931.
- 971 Shelly, D. R., G. C. Beroza, and S. Ide (2007), Non-volcanic tremor and low-
 972 frequency earthquake swarms, *Nature*, 446, 305–307, doi:10.1038/nature05666.
- 973 Six, D. and C. Vincent (2014). Sensitivity of mass balance and equilibrium-line
 974 altitude to climate change in the French alps. *J. Glaciol.* 60, 867–878, doi:
 975 10.3189/2014JoG14J014
- 976 Smith, A.M. (200), Microearthquakes and subglacial conditions, *Geophys. Res. Lett.*,
 977 33(24), L24501.
- 978 Sokal, R. R., and C. D. Michener (1958). A statistical method for evaluating system-
 979 atic relationships. *The University of Kansas Science Bulletin* 38, part 2, 22,
 980 1409-1438.
- 981 Swiss Seismological Service (SED) at ETH Zurich (1983) [Data
 982 set], National Seismic Networks of Switzerland, ETH Zürich,
 983 <https://doi.org/10.12686/sed/networks/ch>
- 984 Thelen, W. A., K. Allstadt, S. de Angelis, S. D. Malone, S. C. Moran, and
 985 J. Vidale (2013). Shallow repeating seismic events under an alpine
 986 glacier at Mount Rainier, Washington, *J. Glaciol.*, 59(214), 345–356,
 987 doi:10.3189/2013JoG12J111.
- 988 Thøgersen, K., H. Sveinsson, J. Scheibert, F. Renard and A. Malthé-Sørensen
 989 (2019), The moment duration scaling relation for slow rupture arises from
 990 transient rupture speeds, *Geophys. Res. Lett.* 46, 12805-12814.
- 991 Thomas, A. M., R. M. Nadeau, and R. Bürgmann (2009). Tremor-tide correlations
 992 and near-lithostatic pore pressure on the deep San Andreas fault, *Nature*, 462,
 993 1048–1051, doi:10.1038/nature08654.
- 994 Thomas, A. M., G. C. Beroza, and D. R. Shelly (2016), Constraints on the source
 995 parameters of low-frequency earthquakes on the San Andreas Fault, *Geophys.*
 996 *Res. Lett.*, 43, 1464-1471, doi:10.1002/2015GL067173.
- 997 Thomason, J.F. and N. R. Iverson (2008), A laboratory study of particle ploughing
 998 and pore-pressure feedback: a velocity-weakening mechanism for soft glacier
 999 beds, *J. Glaciol.* 54, 169-181, <https://doi.org/10.3189/002214308784409008>.

- 1000 Uchida, N. and R. Bürgmann (2019), Repeating earthquakes, *Annu. Rev. Earth*
 1001 *Planet. Sci.*, *47*, 305-332.
- 1002 University of Genova. (1967). Regional Seismic Network of North Western Italy.
 1003 International Federation of Digital Seismograph Networks [Data set].
 1004 <https://doi.org/10.7914/SN/GU>
- 1005 Vernay, M., M/ Lafaysse, P., Hagenmuller, R., Nheili, D., Verfaillie and
 1006 S. Morin (2019). The S2M meteorological and snow cover reanalysis
 1007 in the French mountainous areas (1958 - present) [Data set], AERIS,
 1008 <https://doi.org/10.25326/37>
- 1009 Vincent, C., A. Soruco, D. Six, and E. Le Meur (2009). Glacier thickening and de-
 1010 cay analysis from 50 years of glaciological observations performed on Glacier
 1011 d'Argentière, Mont Blanc area, France, *Ann. Glaciol.*, *50*, 73-79.
- 1012 Vincent, C., and L. Moreau (2016). Sliding velocity fluctuations and subglacial hy-
 1013 drology over the last two decades on Argentière glacier, Mont Blanc area, *J.*
 1014 *Glaciol.* *62(235)*, 805-815. doi:10.1017/jog.2016.35.
- 1015 Vincent C., A., Gilbert, B. Jourdain, L. Piard, P. Ginot, V. Mikhaleiko, P.
 1016 Possenti, E. Le Meur, O. Laarman and D. Six (2020). Strong changes in
 1017 englacial temperatures despite insignificant changes in ice thickness at
 1018 Dôme du Goûter glacier (Mont-Blanc area). *The Cryosphere*, *14*, 925–934.
 1019 <https://doi.org/10.5194/tc-14-925-2020>
- 1020 Walter, J. I., E. E. Brodsky, S. Tulaczyk, S. Y. Schwartz, and R. Pettersson (2011),
 1021 Transient slip events from near-field seismic and geodetic data on a glacier
 1022 fault, Whillans Ice Plain, West Antarctica, *J. Geophys. Res.*, *116*, F01021,
 1023 doi:10.1029/2010JF001754.
- 1024 Walter, J. I., I. Svetlizky, J. Fineberg, E. E. Brodsky, S. Tulaczyk, C. G. Barcheck,
 1025 and S. P. Carter (2015), Rupture speed dependence on initial stress profiles:
 1026 Insights from glacier and laboratory stick-slip, *Earth Planet. Sci. Lett.*, *411*,
 1027 112–120. doi:10.1016/j.epsl.2014.11.025.
- 1028 Wiens, D. A., S. Anandakrishnan, J. P. Winberry, and M. A. King (2008). Simul-
 1029 taneous teleseismic and geodetic observations of the stick-slip motion of an
 1030 Antarctic ice stream, *Nature*, *453(7196)*, 770–775. doi:10.1038/nature06990.
- 1031 Zhao, L., Paul, A., Solarino, S., and RESIF (2018). Seismic network XT:
 1032 CICALPS-2 temporary experiment (China-Italy-France Alps seismic tran-
 1033 sect #2 [Data set], RESIF - Réseau Sismologique et géodésique Français.
 1034 <https://doi.org/10.15778/RESIF.XT2018>.
- 1035 Zoet, L. K., B. Carpenter, M. Scuderi, R. B., Alley, S. Anandakrishnan, C. Marone
 1036 and M. Jackson (2013). The effects of entrained debris on the basal slid-
 1037 ing stability of a glacier, *J. Geophys. Res. Earth Surface* *118*, 656–666.
 1038 doi:10.1002/jgrf.20052.